Chapter 14
Actomyosin Complex

Ian Pepper and Vitold E. Galkin

Abstract Formation of cross-bridges between actin and myosin occurs ubiquitously in eukaryotic cells and mediates muscle contraction, intracellular cargo transport, and cytoskeletal remodeling. Myosin motors repeatedly bind to and dissociate from actin filaments in a cycle that transduces the chemical energy from ATP hydrolysis into mechanical force generation. While the general layout of surface elements within the actin-binding interface is conserved among myosin classes, sequence divergence within these motifs alters the specific contacts involved in the actomyosin interaction as well as the kinetics of mechanochemical cycle phases. Additionally, diverse lever arm structures influence the motility and force production of myosin molecules during their actin interactions. The structural differences generated by myosin's molecular evolution have fine-tuned the kinetics of its isoforms and adapted them for their individual cellular roles. In this chapter, we will characterize the structural and biochemical basis of the actin-myosin interaction and explain its relationship with myosin's cellular roles, with emphasis on the structural variation among myosin isoforms that enables their functional specialization. We will also discuss the impact of accessory proteins, such as the troponin-tropomyosin complex and myosin-binding protein C, on the formation and regulation of actomyosin cross-bridges.

Keywords Myosin · Actin · Actomyosin complex · Thick filament · Thin filament · Muscle contraction

Introduction

The actin-myosin complex is a molecular partnership that sustains the existence of eukaryotes, ranging from amoebas to humans. This wide phylogenetic distribution reflects the functional importance of actomyosin interactions. Although

I. Pepper · V. E. Galkin (✉)
Department of Physiological Sciences, Eastern Virginia Medical School, Norfolk, VA, USA
e-mail: pepperi@evms.edu; galkinve@evms.edu

J. R. Harris, J. Marles-Wright (eds.), *Macromolecular Protein Complexes IV*,
Subcellular Biochemistry 99, https://doi.org/10.1007/978-3-031-00793-4_14

conventionally linked to muscle contraction, the unconventional myosins in other cell types govern numerous processes including cell motility, cargo transport, cytoskeletal organization, and tension sensing (reviewed in (Hartman et al. 2011)). Despite this diversity, the function of actin-myosin interactions can be broadly characterized as supporting movement across many biological scales: from the movement of intracellular cargo along the cytoskeleton to the movement of multicellular organisms powered by muscle contraction. Not surprisingly, all myosins share a general mechanism that involves coupling ATP hydrolysis and actin binding to generate force. The universal transduction of chemical energy into mechanical work is reflected in the conserved myosin head, whose motor domain harbors its ATP- and actin-binding activities. Although sequence identity is less than 20% when comparing sequences of heads of evolutionarily distant myosins, conservation of tertiary structure and functionally critical residues has maintained a general consistency of actin-myosin interactions across the eukaryotic tree of life (Cope et al. 1996; Pasha et al. 2016). The primary sequence differences between motor domains ensure that while the steps involved in the ATPase cycle are the same across the board, the rates and equilibrium constants of those steps are tailored for the functional role of each myosin (Shuman et al. 2014; Sweeney et al. 1998). Myosin tail domains exhibit much greater variability in their architectures, with implications for the myosin molecule's ability to dimerize (reviewed in (Krendel and Mooseker 2005)) as well as recognize and mobilize intracellular cargoes (reviewed in (Lu et al. 2014)). Despite exhibiting different conservation patterns, phylogenetic evidence indicates coevolution of the head and tail domains within the myosin protein family (Korn 2000). In contrast to myosins, muscle and cytoplasmic actin isoforms share >90% sequence identity (Perrin and Ervasti 2010; Vandekerckhove and Weber 1978). Thus, the actin-myosin system involves variable myosin motors operating along a conserved actin track (Robert-Paganin et al. 2020).

In this chapter, we aim to shed light on recent advances in our knowledge of actomyosin interactions and their physiological function. We will begin by surveying the general structural features of actin and myosin proteins, as well as the mechanochemical cycle driven by their interaction. This will lead into a discussion of the structural and biochemical evidence, acquired from a variety of myosin isoforms, about each transition in the cross-bridge cycle. We will highlight the isoform-specific differences within the actin-binding interface in the rigor state, which can explain functional differences in actomyosin interactions. After thoroughly characterizing the actomyosin cross-bridge cycle, we will discuss proteins that regulate actomyosin interactions in a muscle sarcomere. We will conclude by presenting examples of how diverse myosin families carry out a vast number of physiological functions while interacting with highly conserved actin filaments.

General Structural Features of Actin and Myosin

Actin

Overview of the Actin Structure

The motor activity of myosin completely relies on its interaction with actin. Actin represents one of the most abundant proteins in the cellular environment, accounting for roughly 10% of total protein content (Farmer et al. 1983). Prior to transition into its active filamentous state, actin exists in a monomeric or globular form (referred to as G-actin). G-actin is a 43-kDa polypeptide with 375 amino acids that are divided into 4 subdomains (Fig. 14.1a). Starting from the traditional orientation of SD1 (residues 1–32, 70–144, and 338–375) in the lower right quadrant (Fig. 14.1a, blue), the other three subdomains are related to each other as follows: SD2 (residues 33–69) lies just above SD1 (Fig. 14.1a, dark green), SD3 (residues 145–180 and 270–337) is located to the left side of SD1 (Fig. 14.1a, light green), while SD4 (residues 181–269) is directly above SD3 in the upper left (Fig. 14.1a, cyan) (Kabsch et al. 1990). Based on their position within the actin filament, SD1 and SD2 together comprise the outer domain, whereas SD3 and SD4 make up the inner domain. These two domains, connected by a hinge region (residues 137–145 and 335–337), form a so-called cleft which harbors a nucleotide (Fig. 14.1a, brown) and a divalent cation (e.g., Mg^{2+} or Ca^{2+}) (Fig. 14.1a, magenta). All mammalian genomes encode for at least six actin isoforms (reviewed in (Perrin and Ervasti 2010)). Skeletal and cardiac muscles each contain their own α-isoforms, while smooth muscle utilizes α-isoform in vascular tissue and γ-isoform in enteric tissue. The β- and γ-cytoplasmic isoforms are present in non-muscle cells. Comparison of all six mammalian isoforms reveals that 347 of the 375 amino acid positions (92.5%) are identical. This conservation pattern is mirrored when comparing actin orthologs from different species – mammalian cytoplasmic actin is 100% identical to chicken and 90% identical to yeast (Egelman 2001).

The first atomic structure of G-actin was revealed by X-ray crystallography (Kabsch et al. 1990) (Fig. 14.1a) to give rise to the first atomic model of the actin filament (Holmes et al. 1990) based on X-ray diffraction pattern from polymerized actin (referred to as filamentous actin or F-actin). Nearly 20 years later, (Oda et al. 2009) used methodological innovations to obtain an improved X-ray fiber diffraction pattern to reveal the conformational "flattening" of G-actin upon polymerization (Fig. 14.1b), which was confirmed later using cryo-EM (Chou and Pollard 2019; Fujii et al. 2010; Galkin et al. 2015; von der Ecken et al. 2015). The power of cryo-EM has been harnessed in recent years to elucidate the precise molecular details of actin's structural transitions. The near-atomic three-dimensional (3D) cryo-EM reconstructions of F-actin with different bound nucleotides (Chou and Pollard 2019; Merino et al. 2018) showed the structural transitions of individual F-actin subunits that occur upon ATP hydrolysis and phosphate release (Fig. 14.1c and d). They suggest that upon G- to F-actin transition, the flattened conformation of the

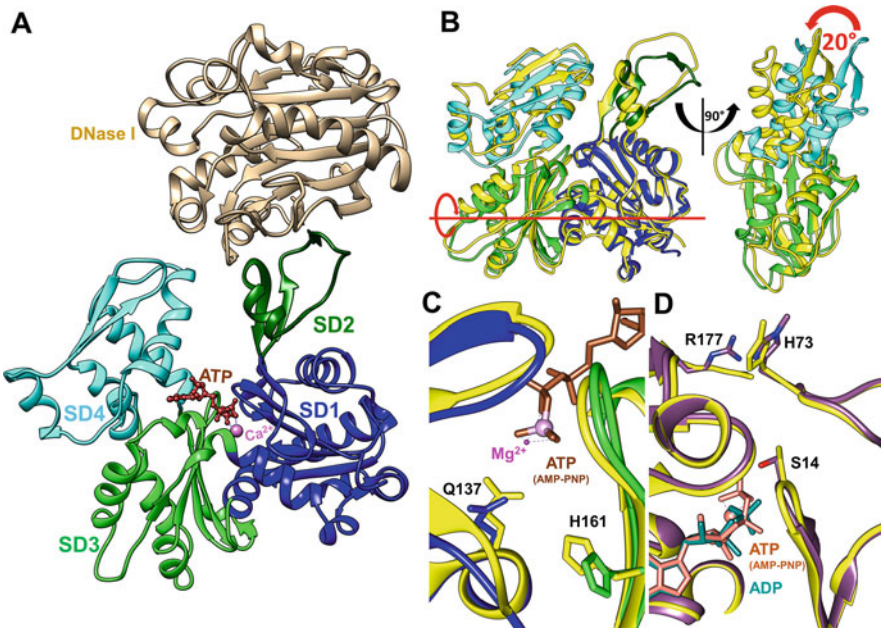

Fig. 14.1 Structure of actin monomers and conformational changes upon polymerization. (**a**) The structure of G-actin is shown using the first crystal structure of G-actin complexed with DNAse I (PDB 1ATN; (Kabsch et al. 1990)). The four subdomains are colored with different shades of green and blue, ATP (brown) and Ca^{2+} cation (magenta) are shown in the ATP-binding cleft. (**b**) Flattening of the actin molecule upon transition from G- to F-actin is shown buy superimposition of G-actin structure (PDB 1ATN; (Kabsch et al. 1990)) shown in (**a**) with the F-actin protomer structure (PDB 6DJM; (Chou and Pollard 2019)) outlined in yellow. To show the "propeller" rotation of the two actin's domains by ~20° (red arrow) around the hinge region (red line) upon flattening of actin the outer domains (e.g., SD1 and SD2) of both structures were aligned. Front (left) and side (right) views are shown. (**c**) Polymerization-induced flattening shifts Q137 and H161 residues, located in actin's cleft, toward the terminal phosphate of bound ATP which facilitates ATP hydrolysis. The same structures and color scheme from (**b**) is utilized. The ATP homologue AMP-PNP used to mimic ATP is shown in brown, while the expected position of γ-phosphate is depicted as plum sphere. (**d**) Conformational changes in the F-actin protomer nucleotide-binding site upon ATP hydrolysis. The ADP-Mg^{2+}-bound actin structure (PDB 6DJO; (Chou and Pollard 2019)) is represented in purple, and actin bound to the ATP analog AMP-PNP (PDB 6DJM; (Chou and Pollard 2019)) is represented in yellow. In the ADP-bound state, the backdoor for phosphate release is open due to interaction between R177 and H73

actin molecule (Fig. 14.1b) results in repositioning of the Q137 and H161 residues closer to the γ-phosphate so that their hydrogen-bonded water molecules are now optimally positioned for ATP hydrolysis (Fig. 14.1c). P_i then exits through a back-door mechanism modulated by more subtle conformational changes of S14, the H73 sensor loop, and R177 (Chou and Pollard 2019; Wriggers and Schulten 1999) (Fig. 14.1d).

Formation of the Actin Filament

Formation of the actin filament (reviewed in (Pollard 2016)) includes three phases: (1) nucleation or formation of oligomers, which is the rate-limiting step; (2) elongation, in which additional monomers are added to the nucleated oligomer; and (3) steady-state, in which the rate of monomer addition at one filament end equals the rate of disassembly at the other end (Fig. 14.2a). The two ends of the filament display asymmetrical polymerization kinetics (Pollard 1986) – whereas filament growth happens at the "barbed"(+) end of filaments, subunit dissociation is mainly localized to the "pointed"(-)end (Fig. 14.2a). The result is end-to-end treadmilling of actin subunits at steady-state, with filaments maintaining a constant average length (Brenner and Korn 1983; Fujiwara et al. 2002; Wegner 1976). The difference in "flattening" of actin molecules upon addition to the filament from either end may explain the differential rate of filament elongation at the ends (Chou and Pollard 2019). To prevent spontaneous polymerization of G-actin in the cell, the formation of actin filaments is controlled by a variety of actin-binding proteins (Fig. 14.2b–d). There are two types of actin monomer-binding proteins (reviewed in (Pollard 2016)): sequestering proteins (e.g., profilin and thymosin-β4), which prevent actin monomers from spontaneous polymerization and nucleation-promoting factors (NPFs). The Wiskott-Aldrich homology 2 (WH2) domain-containing proteins (e.g., WASP) have been shown to promote regulated branching of actin filaments via recruitment of the actin-related proteins 2/3 complex (Arp2/3) (reviewed in (Molinie and Gautreau 2018; Pollard 2007)), while formins have been shown to promote elongation at the ends of the filaments (reviewed in (Courtemanche 2018)). Depolymerization of actin filaments is controlled by severing proteins (e.g., cofilin/ADF and gelsolin) (reviewed in (Pollard 2016)), which maintain the cellular balance between G- and F-actins.

An actin filament consists of two right-handed helices wrapped around each other in a staggered manner, such that lateral subunits on opposite strands are offset by half the monomer length (Fig. 14.3a). Two types of intersubunit contacts maintain actin filament integrity: longitudinal contacts linking the monomers on each strand (Fig. 14.3b–d) and lateral contacts joining both strands together (Fig. 14.3e–f) (Chou and Pollard 2019; Merino et al. 2018; Risi et al. 2021a; von der Ecken et al. 2016; von der Ecken et al. 2015).

Most of the longitudinal interactions between actin protomers are formed between the SD2 of the lower actin and SD1 and SD3 of the upper subunit (Fig. 14.3b and c). The tip of the D-loop of the lower subunit (Fig. 14.3b, blue atoms) makes hydrophobic interactions with residues of the upper subunit that form a hydrophobic cavity between its SD1 and SD3 (Fig. 14.3b, red atoms). Meanwhile, an H-bond links lower protomer's SD2 (Fig. 14.3b, plum atoms) with SD1 of the upper subunit (Fig. 14.3b, orange atoms). Finally, positively charged residues of SD2 of the lower actin (Fig. 14.3c, blue, red, and green atoms) make salt-bridges with the acidic residues of SD3 of the upper subunit (Fig. 14.3c, plum, yellow, and orange atoms). Interactions between SD4 of the lower actin and SD3 of its upper

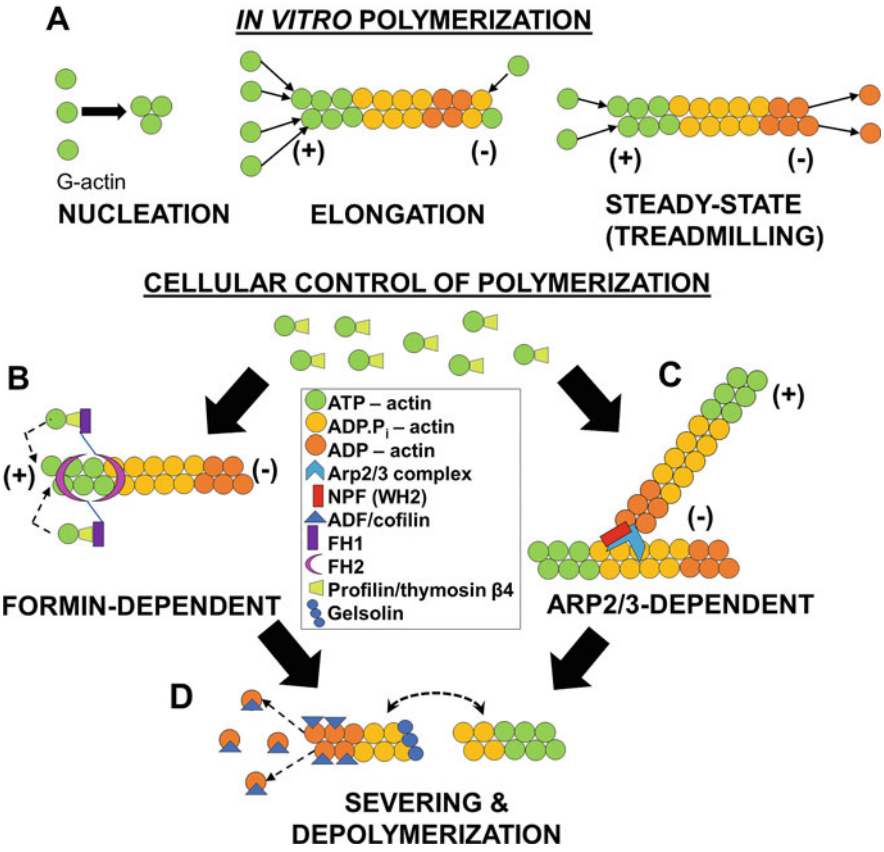

Fig. 14.2 Polymerization of actin filaments. (**a**) Diagram of phases of in vitro polymerization of actin. Following the slow rate-limiting step of G-actin nucleation, filaments are elongated by addition of subunits mostly at the fast-growing barbed (+) end. The bound nucleotide within the incorporated subunits undergoes hydrolysis and subsequent phosphate release. These steps generate an "age-dependent" gradient of nucleotide states along the filament, in which ATP-actin subunits (green) are localized mostly at the barbed end, while ADP-actin subunits (orange) are localized in the center of the filament. Upon reaching equilibrium the filament enters so-called treadmilling, when ATP monomers are added mostly to the filament at the barbed (+) end, while dissociation of the ADP monomers occurs predominantly at the pointed (-) end. (**b–d**) Cellular mechanisms for regulating actin filament polymerization. Free ATP-G-actin (green circles) in the cell is prevented from unregulated polymerization via to its association with actin-sequestering proteins profiling/thymosin β4 (olive green trapezoids). Nucleation and elongation can occur by two distinct mechanisms shown in **b** and **c**. (**b**) Formin-dependent polymerization. Proteins of the formin family (denoted FH1/FH2) can stimulate both nucleation and elongation via dimerization of their formin homology 2 (FH2) domains. The FH2 domain (magenta eclipses) associates with the barbed end, and its linked FH1 domain (plum rectangles) brings G-actin (green circles) complexed with profilin/thymosin β4 (olive green trapezoids) to the barbed (+) end. (**c**) ARP2/3-dependent polymerization. New actin filaments can branch from the side of an existing one. The association of a WH2-containing NPF (red rectangle) and the Arp2/3 complex (cyan chevron) serves as the nucleation seed for the polymerization of actin at the side of the existing filament. (**d**) Severing of filaments can be accomplished by gelsolin (blue circles), which binds to the filament interior and generates a break point. ADF/cofilin (blue triangles) proteins bind to the pointed end of the filament enriched in ADP actin to promote its depolymerization

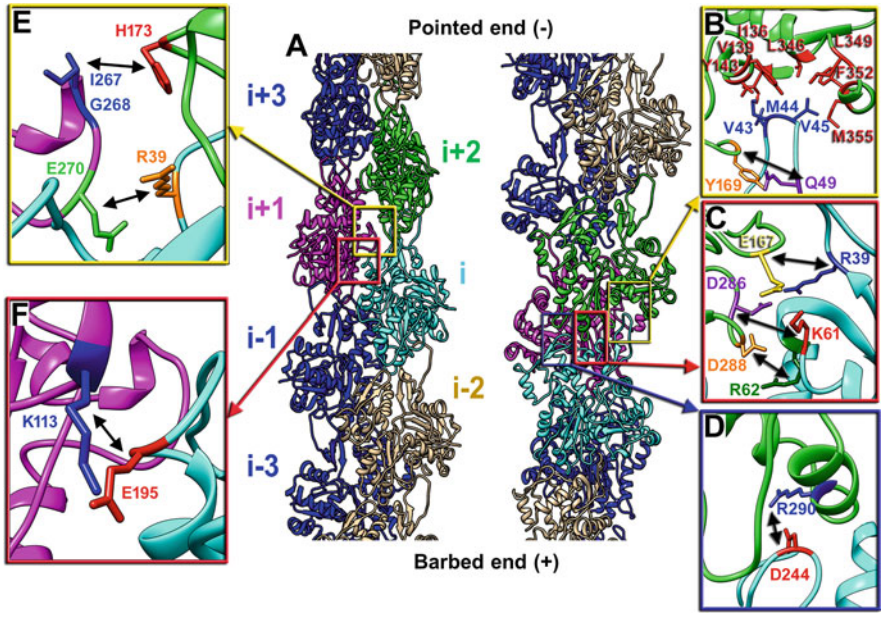

Fig. 14.3 Interactions between actin subunits that hold F-actin. (**a**) Actin filament (PDB 7JH7; (Risi et al. 2021a)) has actin subunits position within the filament labeled as in the basic left-handed one-start helix. The two strands of the actin filament are colored in blue and tan, while subunits which interactions are detailed in (**b**–**f**) are marked in cyan, magenta, and green. (**b–d**) Longitudinal interface is comprised of: (**b**) interactions between the tip of the D-loop (V43, M44, V45, blue) and residues forming a hydrophobic cavity between SD1 and SD3 (I136, V139, Y143, L346, L349, F352, M355 red), along with the Y169 of SD3 (yellow) forming H-bond with Q49 of SD2 (plum); (**c**) salt bridges between R39 (blue), K61 (red), R62 (green) of SD2 and D286 (plum), E167 (yellow), D288 (orange) of SD3, respectively; (**d**) electrostatic interaction between D244 of SD4 (red) of the lower subunit with R290 of SD3 (blue) of the upper subunit. (**e–f**) Lateral interactions are comprised of: (**e**) electrostatic interaction between E270 located in the so-called hydrophobic plug of the i+1 subunit (green) with R39 residing in the SD2 of the i subunit across the strand (orange); hydrophobic interactions between I267/G268 located in the hydrophobic plug of the i+1 subunit (blue) with H173 from the SD2 of the i subunit (orange); (**f**) salt bridge between K113 located in the SD1 of the i+1 subunit (blue) with E195 from the SD4 of the i subunit (cyan). The pairs of amino acids involved in interactions are connected with black arrows

counterpart are held by the salt-bridge between D244 of SD4 (Fig. 14.3d, red atoms) and R290 of SD3 (Fig. 14.3d, blue atoms). The lateral interactions are comprised of a salt bridge between the H-plug and the SD2 of the actin subunit across the strand (Fig. 14.3e, green and orange atoms, respectively). In addition, a lateral contact is formed by the ionic interaction between SD1 and SD4 of the two actins across the strand (Fig. 14.3f, blue and red atoms, respectively).

Myosin

Overview of the Myosin Structure

The myosin polypeptide can be subdivided into its head and tail regions (Fig. 14.4a). The head contains the motor domain (Fig. 14.4a, red), which holds the ATP- and actin-binding sites and represents the most conserved portion among all myosin classes (Cope et al. 1996; Foth et al. 2006). The lever arm (Fig. 14.4a, yellow and green) generates force by converting Ångstrom-scale motor domain conformational changes into nanometer-scale movements (Jontes et al. 1995; Whittaker et al. 1995). The tail (Fig. 14.4a, blue) represents the most variable part of all myosins since its architecture is directly linked to their functionality. For example, membrane-binding tail domains of class I myosins permit them to dynamically regulate membrane-cytoskeleton interactions by sensing intracellular mechanical forces when bound to the actin filament (Fig. 14.4b) (reviewed in (McConnell and Tyska 2010)). While myosin I works as a monomer, other myosins have to form dimers or even filaments via their α-helical coiled-coil domains. For instance, class II muscle myosin forms filaments, in which the coiled-coil rods are packed together in a parallel cylindrical arrangement (Fig. 14.4c) (Al-Khayat et al. 2013; Hu et al. 2016; Kensler and Stewart 1983). On the other hand, class V myosins (e.g., Myosin Va) form a dimer using its tail domain, which also contains a cargo-binding domain (CBD) responsible for transporting its intracellular cargoes (Fig. 14.4d) (Pylypenko et al. 2013; Wu et al. 2002).

Due to the low solubility of the complete myosin molecule under physiological salt concentrations (Margossian and Lowey 1982), water-soluble head fragments generated via enzymatic digestion of muscle myosins have been the main source of knowledge regarding its structure and kinetics. Trypsin segments the molecule in the middle of its tail (Fig. 14.4e, cyan arrow) to generate the heavy meromyosin (HMM) segment containing the head and proximal tail (Mihalyi and Szent-Gyorgyi 1953). HMM can be further digested by papain (Fig. 14.4e, red arrow) to produce the so-called subfragment-1 (myosin-S1), which exclusively contains the motor domain and lever arm regions, and the proximal tail fragment called S2 (Kominz 1965). Isolated myosin-S1 heads (Fig. 14.4e, denoted as S1) can perform as minimal motor units in vitro, as demonstrated by their ability to couple ATP hydrolysis with force generation (Kishino and Yanagida 1988; Toyoshima et al. 1987).

Components of a Myosin-S1 Molecule

The first structure of the myosin-S1 was solved by X-ray crystallography (Rayment et al. 1993). Subsequent analyses of myosin motor domain crystal structures with different nucleotide analogues in their clefts (Dominguez et al. 1998; Fisher et al. 1995b; Houdusse et al. 1999; Houdusse et al. 2000; Rayment et al. 1993) revealed four major subdomains of myosin along with their connecting elements, which are

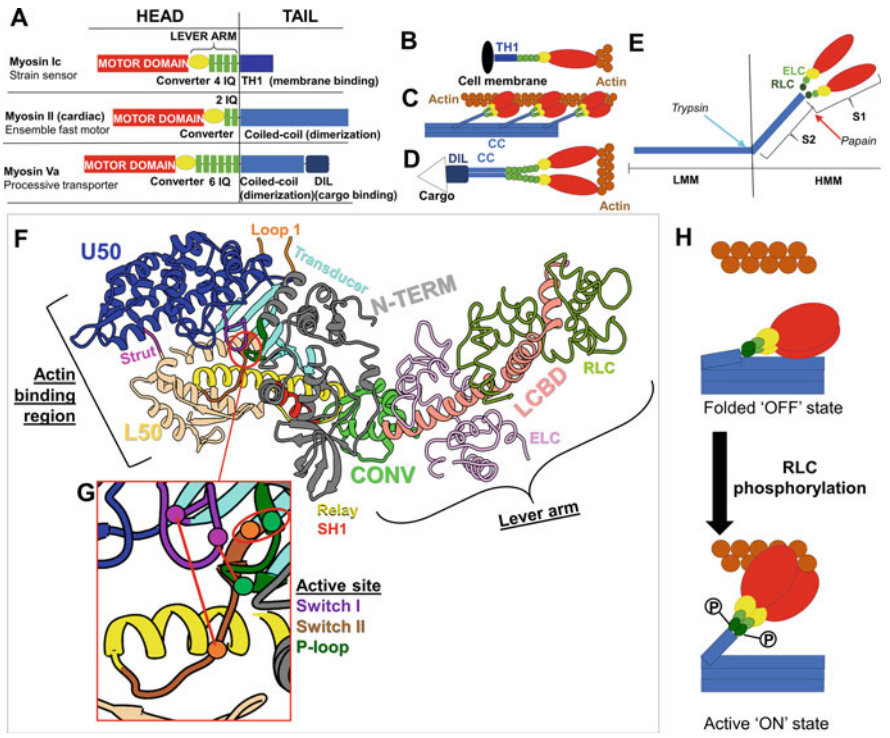

Fig. 14.4 General structural features of myosins. (**a**) Domain organization of different myosin isoforms: myosin Ic (strain sensor), cardiac myosin (ensemble fast motor), and myosin Va (processive transporter). (**b**) Myosin Ic bounds to a cell membrane (black oval) via its tail homology 1 (TH1) domain (dark blue rectangle). (**c**) Cardiac myosin forms thick filaments *via* its Coiled-coil (CC) domain (light blue rectangles) so that protruding motor domains (red ovals) can reach actin-based thin filaments (brown) to generate contractile force. (**d**) Myosin Va forms a dimer via its CC domain to processively transport intracellular cargo (white triangle) recognized by the dilute (DIL) domains (blue box). (**e**) Subdivisions of the muscle myosin heavy chain resulting from enzymatic digestions. (**f**) Components of nucleotide-free myosin-S1 from skeletal muscle (PDB 2MYS; (Rayment et al. 1993)). The motor domain's primary components are: upper (U50; dark blue) and lower (L50; tan) 50 kDa subdomains harboring actin binding interface (black square bracket); N-terminal 25 kDa subdomain (N-term; gray); active site (red circle) containing the ATP-binding elements – P-loop (dark green), switch I (purple), and switch II (brown); strut (magenta); transducer (cyan) with associated loop 1 (orange); relay helix (yellow); SH1 helix (red); converter (green). The terminal helix of the converter extends into light chain-binding domain (salmon), which binds the essential light chain (plum) and regulatory light chain (olive). The converter, LCBD, and bound light chains comprise the lever arm (black square bracket). (**g**) Interactions between residues of active site elements in the nucleotide-free state marked with red lines and oval. (**h**) Phosphorylation of RLC regulates the availability of smooth muscle myosin heads for cross-bridge formation

depicted in Fig. 14.4f. The motor domain of myosin-S1 consists of a central 50 kDa subdomain divided into upper (U50) (Fig. 14.4f, blue) and lower (L50) (Fig. 14.4f, tan) halves, followed by the 25 kDa N-terminal (N-term) subdomain (Fig. 14.4f, gray). Conserved secondary structural elements on the U50 and L50 surfaces

constitute the actin-binding interface (Fig. 14.4f, square bracket). A short linear element known as the strut (Fig. 14.4f, magenta) spans the U50–L50 cleft and assists its closure during myosin's strong binding to actin (Fujita-Becker et al. 2006; Sasaki et al. 2000). At the site of convergence between all three subdomains lies the so-called active ATP-binding site (Fig. 14.4f, red circle, nucleotide-free state is shown). It resides next to the transducer, which is comprised of the seven-stranded β-sheet (Fig. 14.4f, cyan) and its associated loop 1 (Fig. 14.4f, orange) positioned between the U50 and N-term. The active site elements that bind and coordinate ATP are switch I (Fig. 14.4g, purple), switch II (Fig. 14.4g, brown), and the P-loop (Fig. 14.4g, dark green). Structural coupling between the actin-binding region (Fig. 14.4f, square bracket), active site (Fig. 14.4f, red circle), and the lever arm (Fig. 14.4d, curved bracket) is mediated by several myosin elements (Houdusse et al. 2000). The strut (Fig. 14.4f, magenta) links the U50 and L50 actin-binding subdomains together. Switch II, involved in nucleotide binding (Fig. 14.4f, brown), connects the transducer domain (Fig. 14.4f, cyan) with the relay helix (Fig. 14.4f, yellow). The relay helix (Fig. 14.4f, yellow) connects the actin-binding L50 (Fig. 14.4f, tan) with the converter domain (Fig. 14.4f, green). The SH1 helix (Fig. 14.4f, red) bridges the N-term of the motor domain (Fig. 14.4f, gray) with the converter domain at the lever arm base (Fig. 14.4f, green). The mechanism of the allosteric coupling between these elements is discussed below.

The C-terminus of the converter domain gives rise to an alpha-helical extension known as the lever arm helix or "neck" region (Fig. 14.4f, salmon). The neck is also referred to as the light chain-binding domain (LCBD). Each myosin isoform's LCBD binds its light chains via IQ motifs (Fig. 14.4a, green), whose name derives from the isoleucine (I)-glutamine (Q) repeat at the start of their consensus sequence. Sequence variations within these IQ motifs determine the type of the attached light chains (reviewed in (Heissler and Sellers 2014)). Muscle myosins possess a calcium-binding essential light chain (ELC) proximal to the converter (Fig. 14.4f, plum) and a phosphorylation-dependent regulatory light chain (RLC) more distal from the converter (Fig. 14.4f, olive). RLC phosphorylation by a tissue-specific myosin light chain kinase plays an important role for smooth muscle activation (Driska et al. 1981; Pearson et al. 1984). RLC phosphorylation triggers relaxed smooth muscle myosin heads in the "OFF" state to release from the thick filament backbone and become available for cross-bridge formation (Yang et al. 2019) (Fig. 14.4h). RLC phosphorylation can also contribute to activation of the striated muscle myosins (Woodhead et al. 2013; Zhao et al. 2009). "Unconventional" non-muscle myosins exhibit more variability in both their quantity and type of bound light chains (Heissler and Sellers 2014). For example, the neck region of myosin Va is capable of associating with ELCs or calmodulin (CaM), but not RLCs (De La Cruz et al. 2000). CaM light chains regulate myosin Va activity in a calcium-dependent manner (Wang et al. 2004).

The Molecular Mechanisms of the Actomyosin Cross-Bridge Cycle

Overview of the Actomyosin Cross-Bridge Cycle

The actomyosin cross-bridge cycle (Fig. 14.5a) relies on the allosteric coupling between the U50 (Fig. 14.4f, blue) and L50 (Fig. 14.4f, tan) actin-binding subdomains, ATP-binding active site (Fig. 14.4f, red circle), and the lever arm (Fig. 14.4f, curved bracket). This coordinated cross-talk, spanning across the entire myosin-S1, ensures that the biochemical state of the active site (i.e., nucleotide-free, or ATP, ADP.Pi, and ADP-bound) determines the structural conformation of the actin-binding subdomains and the lever arm (reviewed (Houdusse and Sweeney 2016)). The completion of myosin's force-generating powerstroke results in the formation of its so-called rigor interface with actin (Fig. 14.5a, step 1). In this state with the greatest actin affinity, the actin-binding cleft is fully closed (Fig. 14.5b, magenta arrow), the nucleotide-binding active site is empty, and the lever arm occupies its "down" position (Fig. 14.5b, green arrow) (Coureux et al. 2003; Lorenz and Holmes 2010). Execution of a subsequent powerstroke requires ATP binding to myosin. ATP binding weakens the actin-myosin interaction by opening the actin-binding cleft (Fig. 14.5c, magenta arrow) such that the two proteins no longer associate (Conibear et al. 2003) (Fig. 14.5a, light blue arrow), while the lever arm maintains its rigor configuration (Fig. 14.5c, green arrow) resulting in a post-rigor state (Fig. 14.5a, step 2) (Coureux et al. 2004). The next part of the cycle is called a recovery stroke (Fig. 14.5a, dark blue arrow),which is associated with the hydrolysis of ATP into ADP and Pi and reversal of the myosin lever arm (Fig. 14.5d, green arrow) to its Pre-powerstroke state (Fischer et al. 2005; Lombardi et al. 1995; Suzuki et al. 1998) (Fig. 14.5a, step 3). The Pre-powerstroke state is very stable in the absence of actin due to intrinsically slow release of the ADP and Pi. Thus, the Pre-powerstroke state traps ADP and Pi within the myosin active site until formation of the actomyosin complex (Fisher et al. 1995a; Houdusse et al. 2000). The Pre-powerstroke state first associates with actin via electrostatic steering, forming a weakly-bound actomyosin complex that can adopt various configurations (Thomas et al. 1995) (Fig. 14.5a, step 4). This initial association presumably gives rise to the phosphate-release state (PiR) in which Pi leaves the active site (Llinas et al. 2015) (Fig. 14.5a, step 5). PiR state isomerizes into a stereospecific actomyosin complex, which increases the affinity of the two proteins for each other due to the actin-binding cleft closure, and leads to the Pi release and a major lever arm swing (Bershitsky et al. 1997; Eisenberg and Hill 1985; Ferenczi et al. 2005; Houdusse and Sweeney 2016; Kraft et al. 2005; Llinas et al. 2015; Robert-Paganin et al. 2020) (Fig. 14.5a, step 6). These coupled allosteric changes lead to attainment of the strongly bound ADP state (Fig. 14.5a, step 7). The final part of the force-generating powerstroke takes place upon ADP release and is accompanied by a minor lever arm swing (Capitanio et al. 2006; Veigel et al. 1999; Wulf et al. 2016). With myosin strongly bound to actin in a nucleotide-free state, it has again achieved the rigor state (Fig. 14.5a, step 1) and successfully completed a powerstroke. In the following sections, we will discuss those steps in detail.

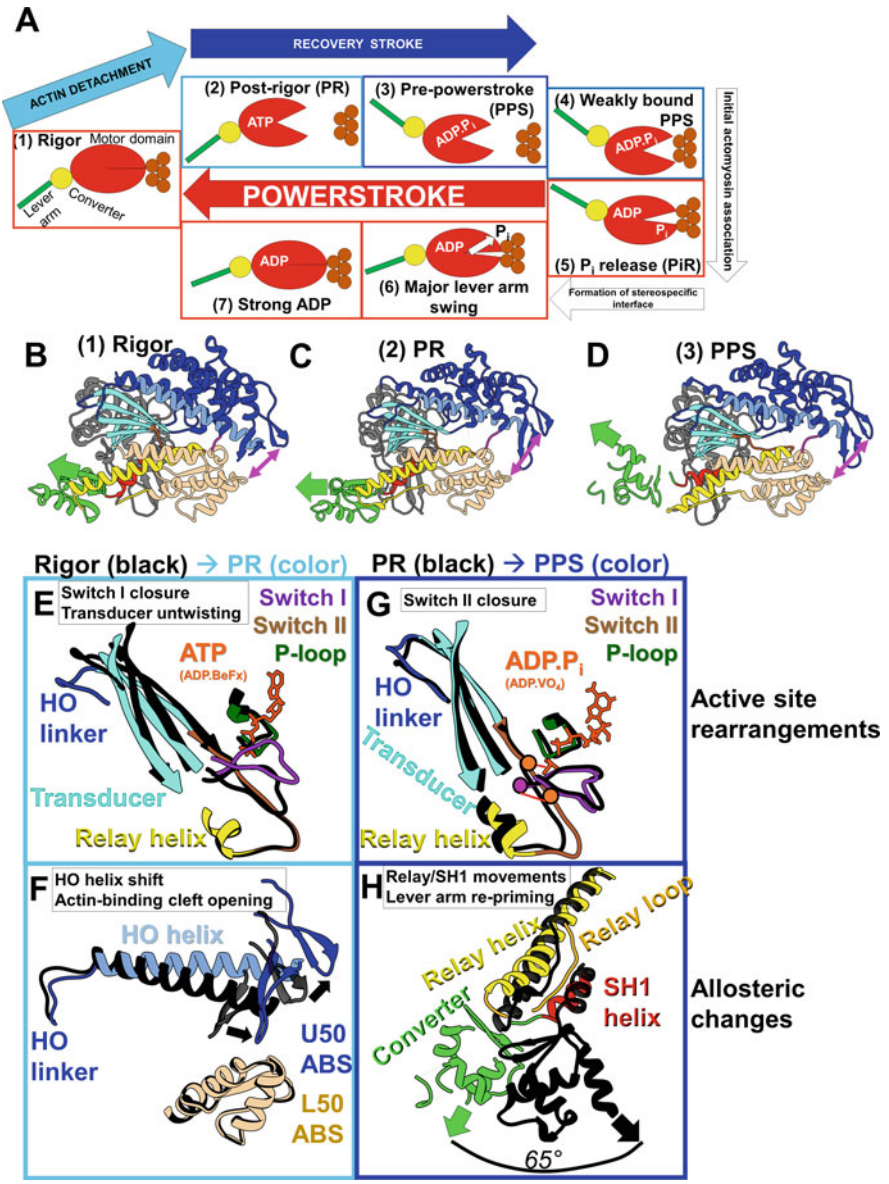

Fig. 14.5 Structural basis of cross-bridge cycle transitions from rigor to pre-powerstroke state. (**a**) Overview of steps involved in one complete actomyosin cross-bridge cycle. Each step of the cycle is marked according to its pace in the set of events required for force generation: red boxes represent steps that are part of the actual power stroke, while the blue boxes represent steps that are prerequisite for a recovery phase of the cycle. (**b–d**) The ribbon diagrams of myosin's major subdomains and connecting elements in are shown for the (**b**) rigor (PDB 1OE9; (Coureux et al. 2003)), (**c**) Post-rigor (PDB 1W7J; (Coureux et al. 2004)), and (**d**) pre-powerstroke (PDB 4ZG4; (Wulf et al. 2016)) states. Magenta double-sided arrows indicate the degree of cleft closure between

ATP-Induced Dissociation of Rigor Actomyosin

Structural studies using X-ray crystals of myosin-S1 with bound ATP homologs (Coureux et al. 2004; Coureux et al. 2003) and biochemical experiments (Conibear et al. 2003; Yengo et al. 2002) firmly established that the transition from the rigor to the post-rigor state (Fig. 14.5a, state (1) to state (2)) results in the opening of the myosin cleft (Fig. 14.5b and c, magenta arrows) and dissociation of myosin from F-actin. Conformational changes in the active site of the motor domain due to ATP binding are allosterically passed through the transducer and HO linker to the actin-binding region (Fig. 14.5e–h). Namely, in the absence of nucleotide, the interactions between the switch I (Fig. 14.4f, purple), switch II (Fig. 14.4f, brown), and the P-loop (Fig. 14.4f, dark green) within the active site (Fig. 14.4g, circled residues) stabilize the closed state of the myosin cleft required for interaction with actin. Entry of ATP (Fig. 14.5e, orange-red) into the empty nucleotide-binding pocket breaks these stabilizing interactions (Coureux et al. 2003; Shuman et al. 2014), which results in transition of the transducer from its "fully twisted" conformation in the rigor state to a "partially untwisted" state in the "post-rigor" state (Fig. 14.5e, transition from black to cyan) (Coureux et al. 2004; Takács et al. 2011; Yang et al. 2007). The alteration of transducer conformation causes a shift in the positioning of the HO linker attached to the N-terminus of the transducer (Fig. 14.5e, transition from black to blue), which in turn tilts the HO helix (Fig. 14.5f, transition from black to light blue). The HO helix (Fig. 14.5b–d, light blue) is a part of the actin-binding U50 domain (Fig. 14.5b–d, blue), hence, its repositioning results in the opening of the myosin cleft (Coureux et al. 2004; Tehver and Thirumalai 2010). The opening of the cleft disrupts the actomyosin interactions that previously held the rigor actomyosin complex.

Fig. 14.5 (continued) the U50 (blue) and L50 (tan) domains, whereas the green arrow shows the orientation of the converter and the lever arm. Within the U50, the HO helix (light blue) links the actin-binding region with the transducer (cyan). (**e–f**) Active site (**e**) and corresponding allosteric actin-binding site (**f**) rearrangements accompanying the rigor to post-rigor (PR) transition. The black ribbons correspond to the rigor state (PDB 1OE9; (Coureux et al. 2003)), while the colored ones represent the post-rigor state (PDB 1W7J; (Coureux et al. 2004)). (**g, h**) Active site rearrangements (**g**) and corresponding allosteric swing of the converter (**h**) accompanying the post-rigor (PR) to pre-powerstroke (PPS) transition. The black ribbons correspond to the PR state (PDB 1W7J; (Coureux et al. 2004)), while the colored ones represent the PPS state (PDB 4ZG4; (Wulf et al. 2016)). Novel interactions of switch II residues (brown circles) with switch I residues (purple circle) and Pi are marked with red lines. During this transition, switch II moves into its closed position (black to brown) and in doing so pulls on the N-terminal of the relax helix (black to yellow). A ~65° rotation of the converter (black to green) is marked with black line between the arrows representing the direction of the lever arm

Recovery Stroke

The current model suggests the following mechanism for transition from the post-rigor to the pre-powerstroke state. During the myosin cleft opening, switch I moves cohesively with U50 from its "open" rigor conformation (Fig. 14.5e, black) to "closed" post-rigor conformation (Fig. 14.5e, purple). This unified movement brings switch I closer to the P-loop (Fig. 14.5e, dark green) and facilitates coordination of the ATP γ-phosphate (Fig. 14.5e, orange-red) (Himmel et al. 2002; Kuhner and Fischer 2011; Reubold et al. 2003). Switch II (Fig. 14.5g, brown) re-forms a salt bridge with switch I in its new conformation, while its glycine residue makes an H-bond with the ATP γ-phosphate (Fig. 14.5g, red lines) (Smith and Rayment 1996). This new "closed" position of switch II (Fig. 14.5g, brown) energetically favors ATP hydrolysis into ADP and Pi (Li and Cui 2004). Since switch II links the active site with the relay helix (Fig. 14.5g, yellow), its movement from "open" to "closed" state results in a cascade of conformational changes involving the relay helix (Fig. 14.5h, transition from black to yellow), its flanking relay loop (Fig. 14.5h, transition from black to gold) and the adjacent SH1 helix (Fig. 14.5h, transition from black to red) (Fischer et al. 2005). As a result of these structural alterations near the interface between myosin motor domain and lever arm, the converter domain (Fig. 14.5d, green) and the attached lever arm (Fig. 14.5d, green arrow) undergo a cumulative ~65° rotation (Fig. 14.5h, black arrow), which completes of the recovery stroke (Blanc et al. 2018; Koppole et al. 2007). The aforementioned closure of switch II also seals the myosin cleft and traps ADP and Pi (Fig. 14.5g, orange-red) in the active site (Fisher et al. 1995b; Houdusse et al. 2000) to protect myosin motor domain from losing its nucleotide before interacting with actin (Shih et al. 2000; Suzuki et al. 1998). ATP-dependent detachment of the myosin molecule from actin and re-priming the lever arm into its pre-powerstroke position is prerequisite for the next powerstroke to occur, which starts from the formation of the weak interactions between the pre-powerstroke myosin molecules and actin.

Initial Actomyosin Association and Pi Release

Due to a lack of actomyosin complex structures for the initial weak-binding state (Fig. 14.5a, step 4), it is impossible to deduce specific actomyosin contacts that mediate it. However, biochemical experiments suggest that the pre-powerstroke state (Fig. 14.6a) forms its initial actomyosin interface via electrostatic interactions involving loop 2 (Fig. 14.6b, red) (Furch et al. 1998; Onishi et al. 2006a), activation-loop (Fig. 14.6b, purple) (Llinas et al. 2015; Varkuti et al. 2012), and to a lesser extent loop 3 (Fig. 14.6b, orange) (Giese and Spudich 1997; Van Dijk et al. 1999). Mutation of conserved lysine residues on loop 2 (Fig. 14.6a, red circles) hinders the rate of initial actomyosin binding (Onishi et al. 2006b), whereas the weak actomyosin state can be strengthened by addition of net positive charge to loop

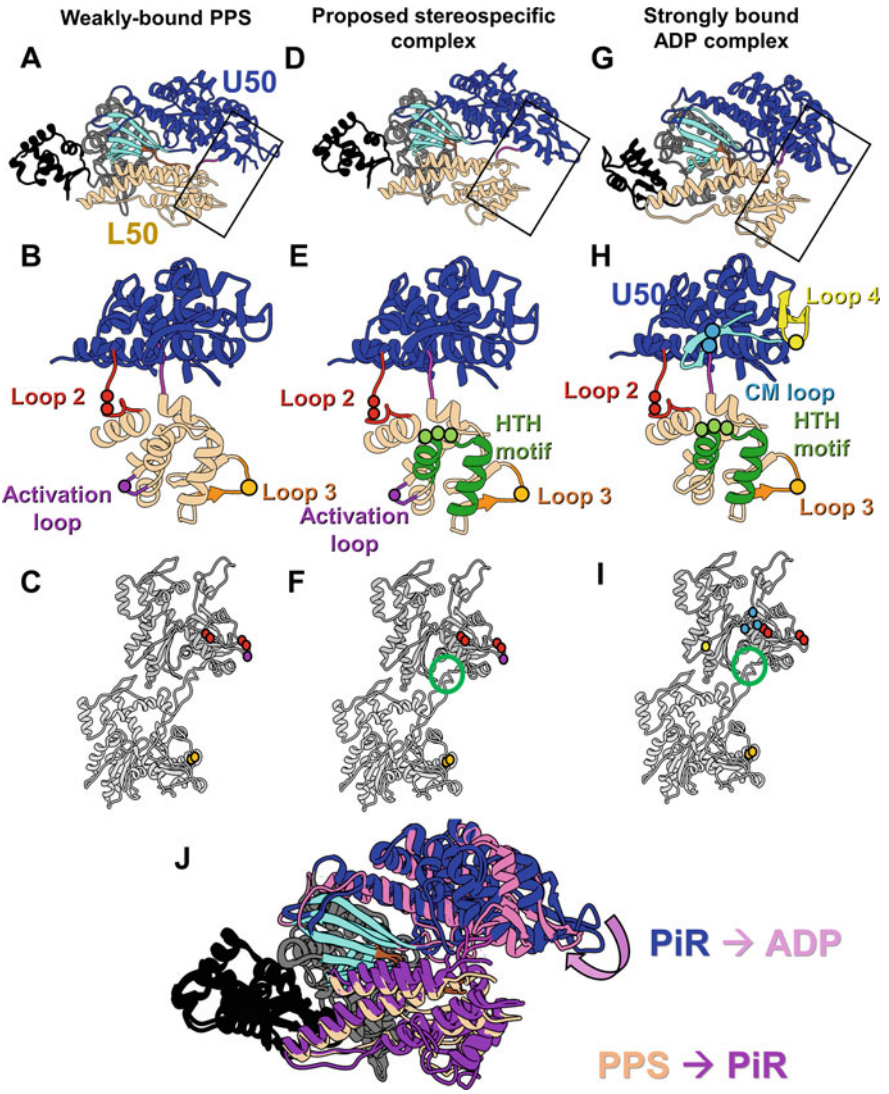

Fig. 14.6 Progressive changes to the actomyosin interface during the force-generating stages of the cross-bridge cycle. The structure and the possible actomyosin interface for the weakly bound pre-powerstroke state (**a–c**) is compared with that of the stereosphesific complex (**d–f**) and finally with the strongly bound ADP actomyosin (**g–i**). The myosin domains are depicted as follows: U50 is blue, L50 is tan, the NTD is gray, converter is black, and transducer is cyan. The black box marks the actin-binding region shown in detail in panels **b**, **e**, and **h**. Panels **c**, **f**, and **i** indicate actin residues that may interact with myosin, while panel **j** shows movements of the U50 and L50 domains upon transitions between the three myosin conformations. (**a**) The structure of the myosin in the pre-powerstroke (PPS) state (PDB 4PK4; (Llinas et al. 2015)). (**b–c**) Surface elements of myosin involved in weakly bound state include loop 2 (red), the activation loop (purple), and loop 3 (orange) (Smith and Rayment 1996). Myosin basic residues (**b**, colored circles) that were proposed (von der Ecken et al. 2016) to form electrostatic interactions with actin acidic residues

2 (Furch et al. 1998; Joel et al. 2001). On the actin side of the interface, relocation of negatively charged residues implicated in the weak-binding state (Fig. 14.6c, red and orange circles) does not impact myosin's progression through its ATPase cycle (Wong et al. 1999). Together, this evidence indicates that initial actomyosin association depends on nonspecific charge complementarity rather than a conserved set of interactions.

In contrast to the ionic interactions maintaining the weak-binding state, the formation of the stereospecific actomyosin interface (Fig. 14.5a, steps 5 and 6) requires both the previously formed electrostatic interactions (Fig. 14.6b and c) and new hydrophobic contacts involving a triplet of residues in the helix-turn-helix (HTH) motif (Fig. 14.6e and f) (Kojima et al. 2001; Onishi et al. 2006a). The structure of the stereospecific actomyosin complex is unknown. Nevertheless, a comprehensive comparison of the cryo-EM structure of rigor actomyosin (Houdusse and Sweeney 2016; von der Ecken et al. 2016) (Fig. 14.5a, step 1) with the crystal structure of myosinin the so-called phosphate-release (Pi-R) state (Fig. 14.5a, step 5) (Llinas et al. 2015) merged with the kinetics data (Muretta et al. 2015) suggests a mechanism of transition from the pre-powerstroke myosin to the stereospecific actin bound state. Loop 2 initiates the interaction of the pre-powerstroke myosin with actin (Furch et al. 1998; Onishi et al. 2006a). The subsequent interaction of the L50 activation-loop (Fig. 14.6b purple), with actin introduces a rotation of the L50 subdomain (Fig. 14.7b, black to tan) that leads to a partial closure of the myosin cleft (Varkuti et al. 2012; von der Ecken et al. 2016) (Fig. 14.6j, PPS to PiR, purple arrow). Due to the rotation of the L50 actin-binding subdomain, switch II moves into its "open" position (Fig. 14.7c, from black to brown) to form a tunnel at the active site's periphery. This tunnel is comprised of residues (Fig. 14.7c, colored circles) that interact with Pi promoting its departure from the active site (Fig. 14.7c, black Pi to plum Pi transition, marked with orange arrow). Switch I (Fig. 14.7c, purple) and the P-loop (Fig. 14.7c, dark green) are coordinated to ADP (Llinas et al. 2015) (Fig. 14.7b, orange-red), while a kinking of the SH1 helix (Fig. 14.7d, red arrow) forms stabilizing interactions with the relay helix (Fig. 14.7d, yellow) and the N-terminal subdomain to keep the converter/lever arm (Fig. 14.7d, green) in its "primed" pre-powerstroke mode (Llinas et al. 2015). Despite the partial closing of the actin-binding cleft in the Pi-release state (Fig. 14.6j, purple arrow), the actin-binding cleft is still not closed enough to form strong interactions with actin. The

Fig. 14.6 (continued) (**c**, same color circles). (**d**) The structure of myosin in the proposed stereospecific complex (PDB 4PFO; (Llinas et al. 2015)). (**e–f**) In the stereospecific actomyosin complex, in addition to interactions shown in **b–c**, the HTH motif (**e**, green) interacts with hydrophobic cavity between two actin subunits (**f**, green circles). The HTH motif interacts with a (green circle). (**g**) The structure of myosin-ADP that forms strongly bound complex with actin (PDB 6C1D; (Mentes et al. 2018)). (**h–i**) In addition to interactions proposed for stereospecific complex, in strongly bound ADP complex CM loop (cyan) and loop 4 (yellow) residues (**h**, colored circles) form contacts with actin residues from SD1/SD3 (**i**, same color circles). (**j**) Sequential movements of the actin-binding region during transitions from weakly to strongly bound myosin

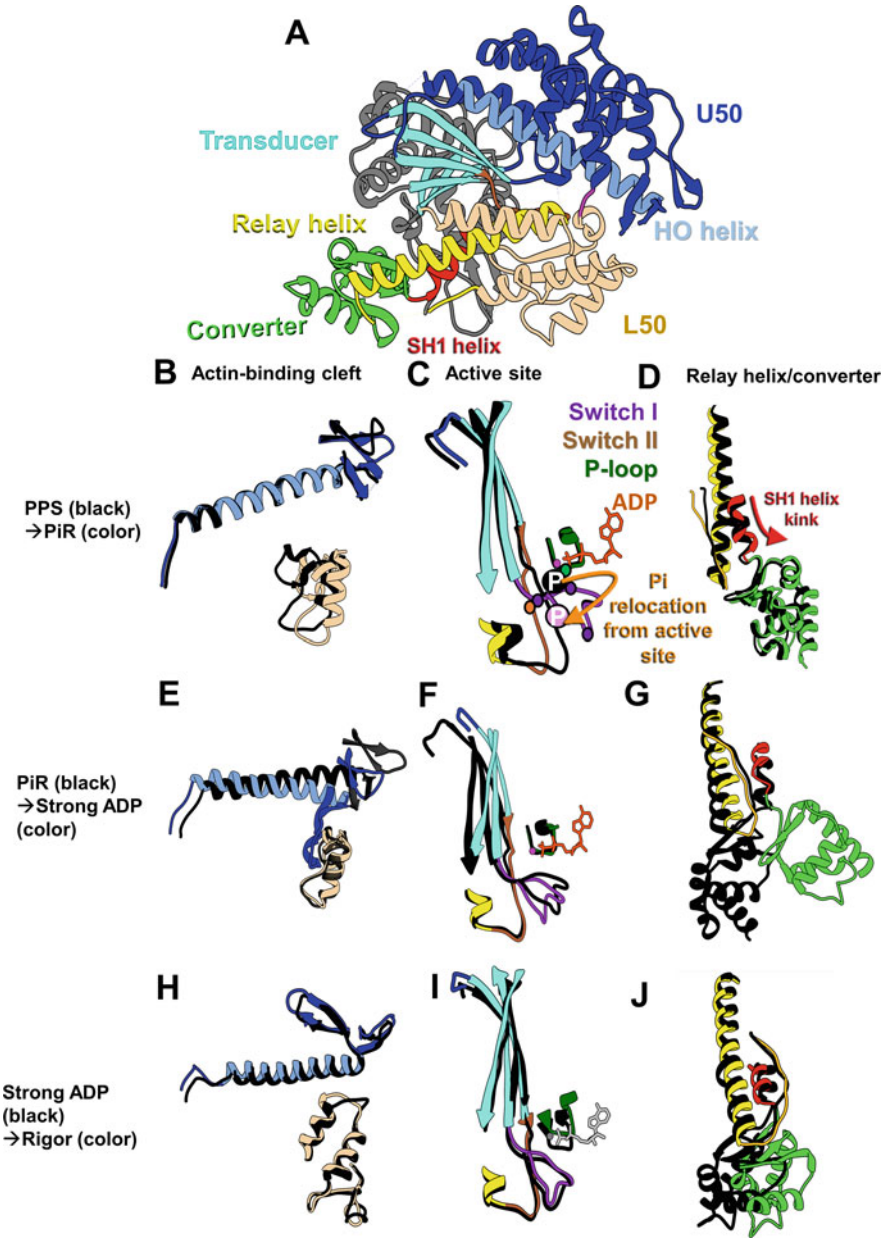

Fig. 14.7 Structural changes within myosin's three allosteric regions that accompany the force-generating powerstroke. (**a**) Schematic of the major domains and their connecting elements in the rigor state of myosin (PDB 1OE9; (Coureux et al. 2003)) are colored as in Figs. 14.4 and 14.5. Detailed views of the allosterically coupled conformational changes in the actin binding cleft (**b, e**, and **h**), active site (**c, f**, and **i**), and relay/converter (**d, g**, and **j**) upon progression of the power stroke from PPS to PiR (**b–d**), from PiR to strong ADP (**e–g**), and, finally, from strong ADP to rigor (**h–j**) are shown using the following structures: PDB 4PK4/4PFO (Llinas et al. 2015), PDB 6BNQ (Gurel

current model suggests that the weak actomyosin interactions facilitate the formation of the stereospecific actomyosin complex (Fig. 14.6d–f), which presumably forms right after the Pi dissociation from the active site (Fig. 14.7c, orange arrow) and requires the interaction of the triplet of residues in the HTH motif (Fig. 14.6e, green) with actin residues forming a hydrophobic cavity at the longitudinal actin interface (Fig. 14.6f, green circle) (Varkuti et al. 2012; von der Ecken et al. 2016). The formation of the stereospecific complex promotes the full closure of the U50-L50 cleft (Fig. 14.6j, pink arrow), which places the HCM loop (Fig. 14.6h, cyan) and loop 4 (Fig. 14.6h, yellow) in proximity to their binding sites on actin (Fig. 14.6h–i) (Gurel et al. 2017; von der Ecken et al. 2016). This leads to the formation of the strongly bound ADP actomyosin complex (Fig. 14.5a, step 6). Upon this transition the HO helix moves backward (Fig. 14.7e, from black to blue) from its position in the post-powerstroke state (Fig. 14.5f, light blue). Since the HO helix is linked to the transducer, the transducer (Fig. 14.7f, from black to cyan) and its associated switch I (Fig. 14.7f, from black to purple) also undergo conformational changes that close the Pi-binding tunnel to prevent Pi reentry. Since the aforementioned alterations in the myosin molecule are coupled with the major movement of the converter domain and lever arm (Fig. 14.7g, from black to green) via the straightening of the relay helix (Fig. 14.7g, from black to yellow) (Muretta et al. 2015), the closure of the Pi binding tunnel makes the powerstroke irreversible (gated).

Fig. 14.7 (continued) et al. 2017), and PDB 6C1D (Mentes et al. 2018). (**b–d**) Allosteric changes in myosin associated with the PPS (black) to PiR (color) transition. (**b**) Rotation of the L50 subdomain (black to tan) partially closes the actin-binding cleft. (**c**) Movement of switch II (black to brown) facilitates the relocation of Pi from the active site (orange arrow) to a binding tunnel comprised of residues from the active site elements (purple, green, and orange circles). (**d**) The SH1 helix (red) is kinked in the Pi release state (red arrow), which allows the SH1 helix (red), relay helix (yellow), and N-term subdomain (not shown) to form interactions that maintain the primed position of the converter/lever arm (green) as seen in the pre-powerstroke state (black). (**e–g**) Allosteric changes in myosin associated with the PiR (black) to strong ADP (color) transition. (**e**) Shift in the HO helix (black to light blue) produces a downward rotation of U50 actin-binding surface (black to blue), thus fully closing the actin-binding cleft. (**f**) Twisting of the transducer (black to cyan) and movement of switch I (black to purple) results in the exit of Pi from myosin. (**g**) Movements of the relay (yellow) and SH1 (red) helices produce the converter rotation (black to green) which is responsible for the major lever arm swing. (**h–j**) Allosteric changes in myosin associated with the strong ADP (black) to rigor (color) transition. (**h**) The orientation of the U50 (blue) and L50 (tan) actin-binding subdomains is unchanged. (**i**) Movement of the P-loop (black to dark green) as well as the transducer β-sheets (black to cyan) induces release of ADP (light gray). (**j**) Conformational changes in the relay (yellow) and SH1 (red) helices result in a rotation of the converter/lever arm (green) to its rigor orientation

ADP Release and Formation of Rigor Complex

The combination of complete actin-binding cleft closure, Pi release, and major lever arm swing places myosin in its strongly bound ADP state (Fig. 14.5a, step 7). In contrast to the ATP-bound post-rigor state with an open actin-binding cleft, the strong-ADP state features a fully closed cleft (Fig. 14.7h) along with tight coordination of nucleotide (Fig. 14.7i, gray atoms). Release of ADP is the final step required for force generation, thus completing one full actomyosin ATPase cycle and placing myosin back in its rigor state (Fig. 14.5a, step 1). Nucleotide release is accomplished by distortions of the transducer sheets (Fig. 14.7i, from black to cyan) which consequently distance the P-loop (Fig. 14.7i, from black to dark green) from switch 1 (Fig. 14.7i, from black to purple) (Wulf et al. 2016). While the transducer rearrangement of the strong-ADP to rigor transition does not affect the positioning of the U50 (Fig. 14.7h, blue) or L50 (Fig. 14.7h, tan) actin-binding subdomains, it alters the orientation of the relay (Fig. 14.7j, from black to yellow) and SH1 (Fig. 14.7i, from black to red) helices, which results in a minor (~9.5°) lever arm swing (Fig. 14.7j, from black to green) (Wulf et al. 2016).

The interface between the motor domain and the lever arm can influence the ADP release step and its associated lever arm swing. This is demonstrated by myosin Ib, which increases its actin attachment lifetime by 75-fold in response to a 2 pN force. Its remarkable tension sensitivity results from stalling the second lever arm rotation associated with ADP release (Laakso et al. 2008). High-resolution structures of myosin Ib ADP-bound and rigor states unveiled a functionally critical hydrophobic pocket at the junction of the converter and lever arm helix. In the ADP-bound state (Fig. 14.8a), loop 5 of the N-term (Fig. 14.8b, gray) docks within this pocket, thus hindering rotation of the lever arm helix (Fig. 14.8b, green) in the presence of high mechanical loads (Mentes et al. 2018). Upon lever arm rotation (Fig. 14.8c), the N-terminal extension (Fig. 14.8d, pink) of myosin Ib is no longer sterically blocked from this pocket, and its association with the lever arm helix (Fig. 14.8d, green) drives the N-term domain rotation required for ADP release (Mentes et al. 2018). This proposed structural mechanism fits with kinetic data, which demonstrates that deletion of the myosin Ib N-terminal extension delays ADP release nearly tenfold (Shuman et al. 2014). In contrast to the lever arm movement, the actin-binding interface undergoes minimal changes during the strong ADP to rigor transition (Fig. 14.8e) (Gurel et al. 2017; Mentes et al. 2018; Wulf et al. 2016). The specific contacts maintaining the rigor interface have been visualized at near-atomic resolution and are discussed in detail within the following section.

The Structure of the Rigor Complex

Our structural knowledge of the actomyosin complex is limited to the strong ADP (Fig. 14.5a, step 7) and rigor (Fig. 14.5a step 1) states. For the rigor state, several

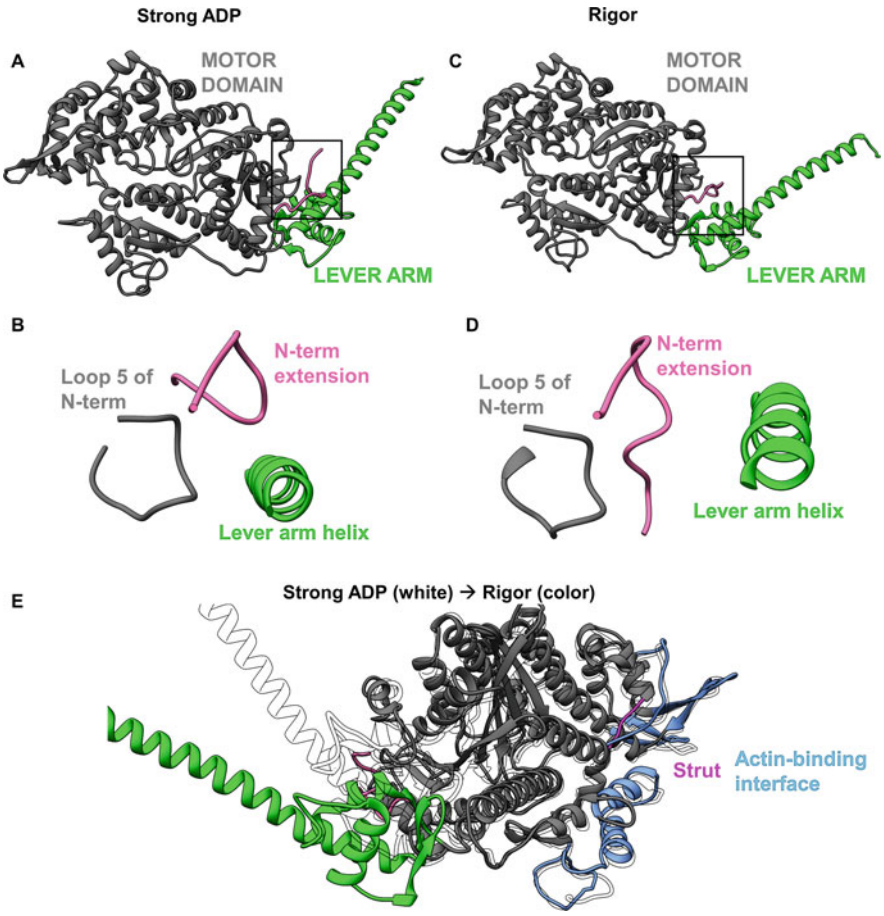

Fig. 14.8 Structural basis of the force-sensitive strong ADP to rigor transition in myosin Ib. (**a** and **c**) Conformations of the motor domain (gray), converter/lever arm (green), and N-terminal extension (pink) in the strong ADP state (PDB 6C1D; (Mentes et al. 2018)) (**a**) and rigor state (PDB 6C1H; (Mentes et al. 2018)) (**c**). The boxed region indicates the interface between the motor domain and converter/lever arm that is depicted in panels **b** and **d**. (**b**) In the presence of mechanical forces restraining the rotation of the myosin Ib lever arm, loop 5 element of the N-terminal subdomain (gray) is buried within a hydrophobic pocket at the base of the lever arm helix (green), while the N-terminal extension (pink) is located outside of this hydrophobic pocket. (**d**) Upon lever arm rotation, the N-terminal subdomain N-terminal extension (pink) moves to a position that sterically prevents the interaction of loop 5 (gray) with the lever arm helix (green), while promotes ADP release. (**e**) Comparison of the major domain orientations in the myosin Ib strong ADP (white) and rigor (color) states. The converter and lever arm undergo a downward rotation that completes the powerstroke (white to green). Since the actin-binding cleft remains fully closed during this transition, the actin-binding interface is relatively unchanged (white to light blue)

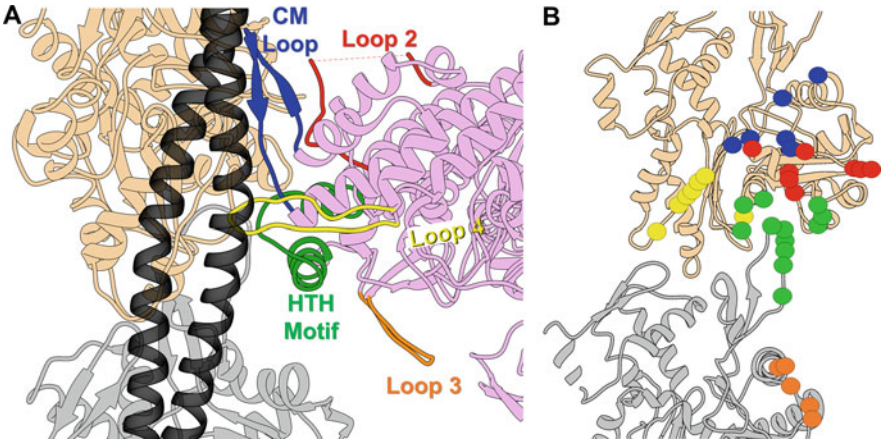

Fig. 14.9 General molecular details of the rigor actomyosin interface. (**a**) Atomic model of the cardiac actomyosin complex in the rigor state (PDB 7JH7, (Risi et al. 2021a)). The myosin motor domain is colored in plum, while the two consecutive actin subunits along the actin filament long-pitch helix that form myosin-binding interface are shown in tan and gray. The tropomyosin cable regulating myosin's access to its binding site of the actin filament is black. The secondary structural elements of the actin-binding region of myosin are presented using primary colors: CM loop (blue), loop 2 (red), loop 4 (yellow), HTH motif (green), and loop 3 (orange). (**b**) Aggregated myosin footprint on the actin surface derived from actomyosin complexes of cardiac myosin (PDB 7JH7, (Risi et al. 2021a)), myosin IIC (PDB 5JLH; (von der Ecken et al. 2016)), myosin VI (PDB 6BNP; (Gurel et al. 2017)), and myosin Ib (PDB 6C1H; (Mentes et al. 2018)). Colored circles represent actin residues, which interact with myosin in aforementioned rigor actomyosin complexes. The color of each circled actin residue corresponds to the myosin actin-binding element (shown in panel **a**) that interacts with it

actomyosin complexes have been visualized by cryo-EM at near-atomic resolution, which allowed unambiguous mapping of the side chains of amino acids comprising the main actomyosin interactions (Fig. 14.9a). This set of structures includes cardiac myosin (3.8 Å; (Risi et al. 2021a)) and myosin IIC (3.9 Å; (von der Ecken et al. 2016))—representing the class II myosins—as well as myosin VI (4.6 Å; (Gurel et al. 2017)) and myosin Ib (3.9 Å; (Mentes et al. 2018))—representing the "unconventional" myosins. Comparison of these four isoforms altogether reveals that in the Rigor state, the actin-binding elements (Fig. 14.9a, primary colors) of myosin (Fig. 14.9a, plum) generally interact with SD1 and SD3 of the upper actin (Fig. 14.9a, tan) as well as SD2 and SD1 of the lower actin (Fig. 14.9a, gray). The core of the "actin footprint" shared by numerous myosins is formed by interactions with the CM loop (Fig. 14.9b, blue circles), HTH motif (Fig. 14.9b, green circles), and loop 2 (Fig. 14.9b, red circles) that are responsible for global positioning of the motor on its actin track. Peripheral contributions from loop 4 (Fig. 14.9b, yellow circles) and loop 3 (Fig. 14.9b, orange circles), which are variable among the myosin isoforms, can optimize the specific details of the actomyosin interaction. By examining the actin side of the interface (Fig. 14.9b, detailed in Figs. 14.10, 14.11, 14.12, 14.13, and 14.14), one can clearly observe a consistent "zone" of actin interactions

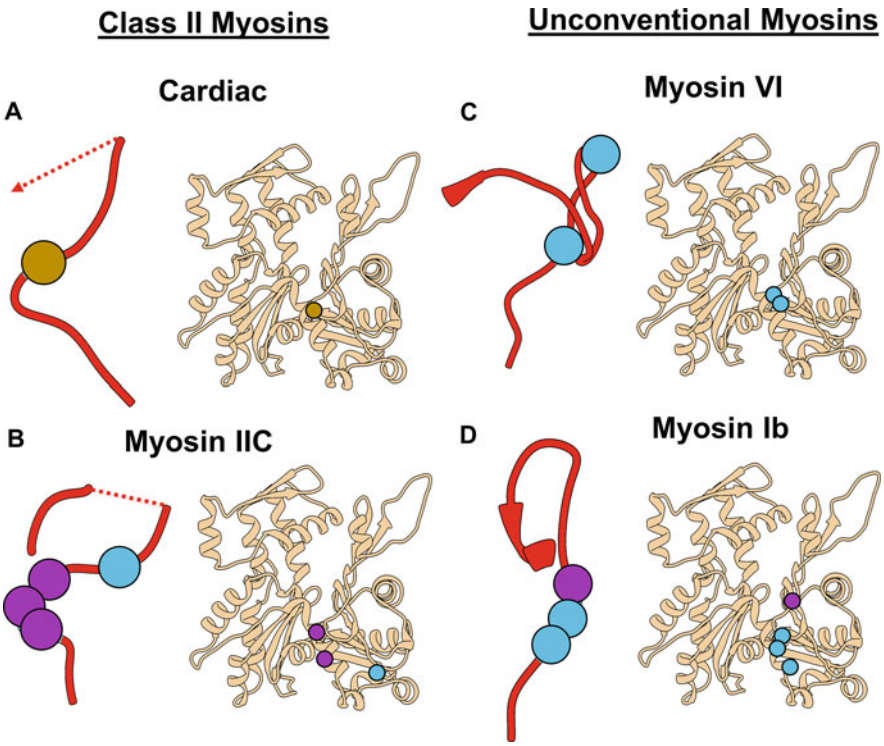

Fig. 14.10 Interactions of loop 2 of myosin with actin observed in conventional and unconventional actomyosin complexes differ. Loop 2 of myosin is red, while actin subunit from Fig. 14.9 is shown in tan. Residues of myosin and actin observed to interact are depicted using symbols of the same color and shape. (**a**) Loop 2 of cardiac myosin (PDB 7JH7, (Risi et al. 2021a)) has the weakest interaction with actin by forming one hydrogen bond with actin SD1 (brown circles). (**b**) Loop 2 of myosin IIC (PDB 5JLH; (von der Ecken et al. 2016)), in addition to a set of hydrophobic interactions with actin at its base (purple circles), makes an electrostatic interaction with the actin N-terminus (blue circles). (**c**) Loop 2 of myosin VI (PDB 6BNP; (Gurel et al. 2017)) has only electrostatic interactions with actin *via* its basic residues interacting with an acidic patch of actin located in SD1 (blue circles). (**d**) Loop 2 of myosin Ib (PDB 6C1H; (Mentes et al. 2018)) forms a mixture of electrostatic (blue circles) and hydrophobic (purple circles) interactions with actin SD1

across the isoforms despite the variations of the participating myosin surface elements.

Loop 2 (Fig. 14.9a, red) exhibits substantial variations in length and flexibility among myosin isoforms, as demonstrated by the cryo-EM structures (Fig. 14.10a–d). Positively charged residues of loop 2 form the initial actomyosin interactions (Fig. 14.6b, c) (Furch et al. 1998; Onishi et al. 2006a). Interestingly, for all examined myosin isoforms except cardiac, these ionic bonds also exist in the rigor state. Basic residues of loop 2 in myosins IIC, VI, and Ib interact with acidic patches within actin SD1 (Fig. 14.10b–d, blue circles). Additionally, in myosin IIC a hydrophobic cluster

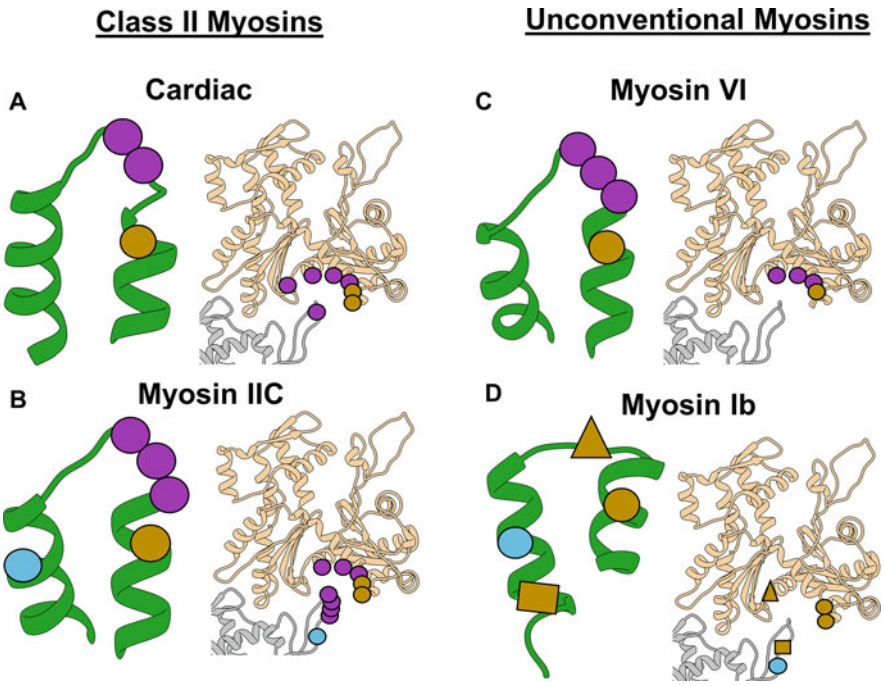

Fig. 14.11 Interactions of HTH motif of myosin with actin are conserved in conventional and unconventional actomyosin complexes except for myosin Ib. HTH motif of myosin is in green, while the two subunits of the actin filament (from Fig. 14.9) are depicted in tan and gray. Residues of myosin and actin observed to interact are depicted using symbols of the same color and shape. (**a**) HTH motif of cardiac myosin (PDB 7JH7, (Risi et al. 2021a)) interacts with a hydrophobic cavity formed by residues in SD1/SD3 of upper actin and SD2 of lower actin (purple circles). A hydrogen bond exists between the N-terminal helix of HTH motif and actin SD1 (brown circles). (**b**) HTH motif of myosin IIC (PDB 5JLH; (von der Ecken et al. 2016)) interacts with a hydrophobic cavity formed by residues in SD1/SD3 of upper actin and SD2 of lower actin (purple circles), while a hydrogen bond exists between the N-terminal helix of HTH motif and actin SD1 (brown circles). In addition, electrostatic interaction exists between the C-terminal helix of HTH motif and actin SD2 (blue circles). (**c**) HTH motif of myosin VI (PDB 6BNP; (Gurel et al. 2017)) makes a set of hydrophobic interactions with actin (purple circles), and forms a hydrogen bond between the N-terminal helix of HTH motif and actin SD1 (brown circles). (**d**) The interactions of the HTH motif of myosin Ib with actin (PDB 6C1H; (Mentes et al. 2018)) are very different from the above-mentioned isoforms: it forms H-bonds with SD1 (brown circles) and SD3 (brown triangles) of the upper actin (tan) as well as SD2 (brown rectangles) of the lower actin (gray). Additionally, an electrostatic contact is formed between the C-terminal helix of HTH motif and actin SD2 (blue circles).

of residues at the loop 2 base interacts with the "hinge" region between SD1 and SD3 (Fig. 14.10b, purple circles). These hydrophobic interactions may also exist for myosin VI but cannot be confirmed due to structural variability of its loop 2 (Gurel et al. 2017). Myosin Ib loop 2 can also hydrophobically interact with actin, due to a unique leucine residue located next to the conserved positively

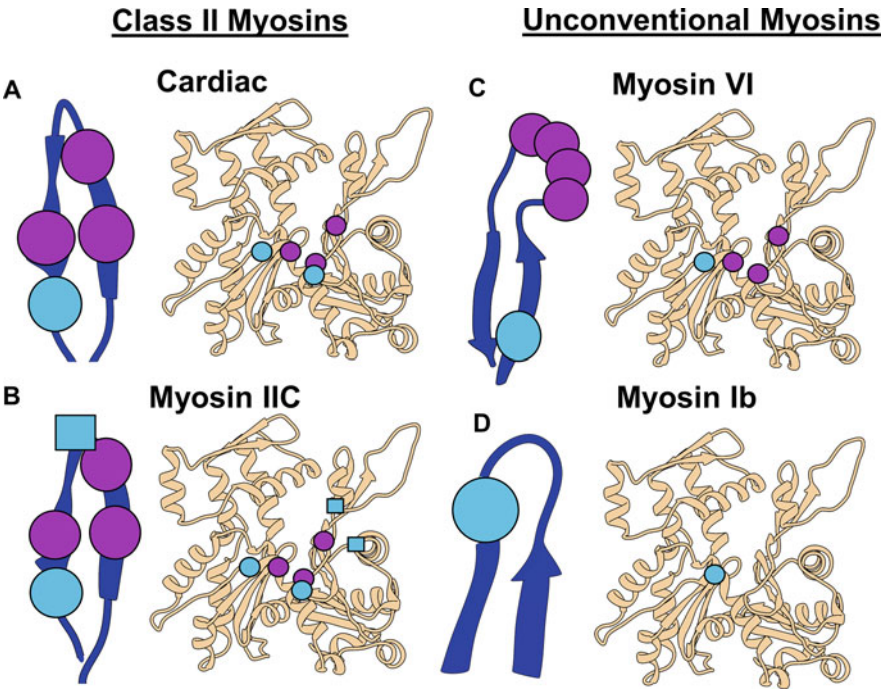

Fig. 14.12 The interface between CM loop of rigor myosin and actin observed in conventional and unconventional actomyosin complexes is different. CM loop of myosin is in blue, while actin subunit from Fig. 14.9 is tan. Residues of myosin and actin observed to interact are depicted using symbols of the same color and shape. (**a**) CM loop of cardiac myosin (PDB 7JH7, (Risi et al. 2021a)) forms hydrophobic interactions with a pocket near the actin SD1/SD3 junction (purple circles), while basic residue at its base interacts with acidic residues on actin SD1 and SD3 (blue circles). (**b**) CM loop of myosin IIC (PDB 5JLH; (von der Ecken et al. 2016)) forms similar hydrophobic interactions with actin (purple circles). In addition, basic residue at its base interacts with acidic residues on actin (blue circles). Additional salt bridge between the tip of myosin IIC CM loop and SD1/SD2 of actin is formed (blue squares). (**c**) Residues in the CM loop of myosin VI (PDB 6BNP; (Gurel et al. 2017)) form a set of hydrophobic interactions with actin residues near the SD1/SD3 junction (purple circles). In addition, basic residue at the CM loop base interacts with an acidic residue on actin SD3 (blue circles). (**d**) The CM loop of myosin Ib (PDB 6C1H; (Mentes et al. 2018)) forms just one electrostatic interaction between its tip and the hinge region of actin (blue circles)

charged region (Fig. 14.10d, purple circles). Loop 2 of cardiac myosin displays attenuated actin interactions relative to the other isoforms as a single hydrogen bond with actin residue maintains this interface (Fig. 14.10a, brown circles).

After the initial actin interactions with loop 2 have formed, the HTH (Fig. 14.9a, green) is brought close to its binding site at actin's hydrophobic groove (Fig. 14.6f, green circle) with assistance from the activation loop (Fig. 14.6e, purple). This process is critical for the transition from a weakly bound to stereospecific actomyosin complex, which in turn facilitates the structural transitions that bring the complex into its rigor state. In sharp contrast to the variability displayed by loop

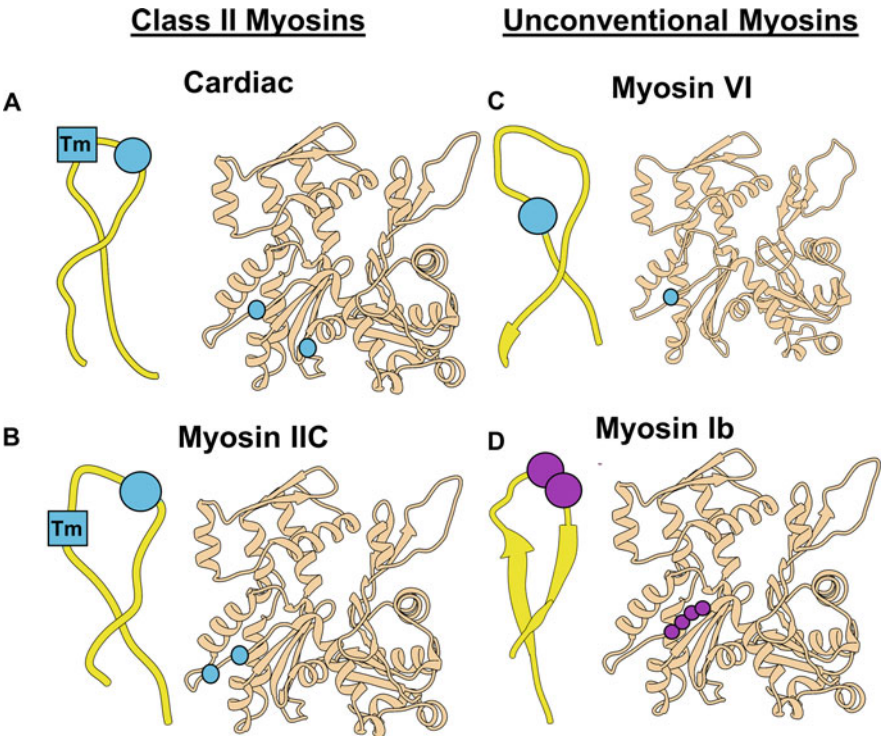

Fig. 14.13 The interactions of loop4 of rigor myosin with actin varies between the actomyosin complexes. Loop 4 of myosin is depicted in yellow, while actin subunit from Fig. 14.9 is tan. Residues of myosin and actin observed to interact are depicted using symbols of the same color and shape. (**a** and **b**) Loops 4 of cardiac myosin (PDB 7JH7, (Risi et al. 2021a)) and myosin IIC (PDB 5JLH; (von der Ecken et al. 2016)) contain acidic residues at their tips that form salt bridges with actin SD3 (blue circles). In addition, loop 4 in both isoforms electrostatically interacts with the regulatory tropomyosin (Tm) cable (blue squares). (**c**) Loop 4 of myosin VI (PDB 6BNP; (Gurel et al. 2017)) forms a salt bridge with actin SD3 (blue circles). (**d**) Loop 4 of myosin Ib (PDB 6C1H; (Mentes et al. 2018)) forms a unique set of hydrophobic interactions between its tip and a hydrophobic cluster in actin SD3 (purple circles)

2, the HTH motif represents the most conserved part of the actomyosin interface. In the HTH of all four myosin isoforms, a conserved glutamic acid residue in the N-terminal helix forms an H-bond with actin SD1 (Fig. 14.11a–d, brown circles). Additionally, all isoforms except myosin Ib feature hydrophobic interactions of the HTH turn with upper actin SD1 and SD3 and the lower actin's D-loop (Fig. 14.11a–c, purple circles). Biochemical mutagenesis studies have confirmed the importance of these conserved hydrophobic residues for myosin's ATPase activity and motility (Onishi et al. 2006a). For myosin Ib, the HTH interface lacks hydrophobic interactions, which are substituted by a set of hydrogen bonds (Fig. 14.11d, brown squares and triangles). Similar to myosin IIC, the Ib isoform makes a salt bridge with the D-loop (Fig. 14.11d, blue circles).

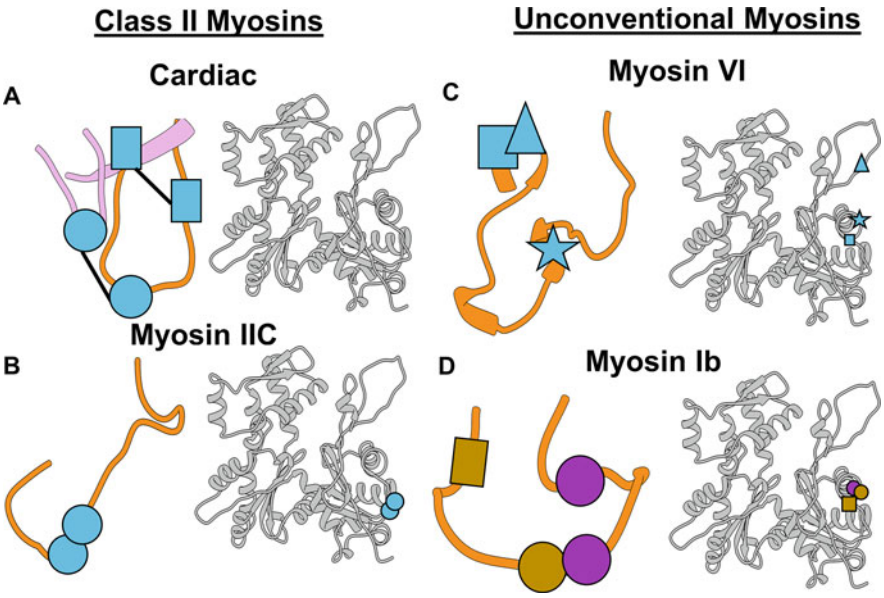

Fig. 14.14 Loop 3 of cardiac myosin does not interact with actin, while all the other isoforms make non-conserved interactions with actin in rigor actomyosin. Loop 3 of myosin is in orange, while actin subunit from Fig. 14.9 is in gray. Residues of myosin and actin observed to interact are depicted using symbols of the same color and shape. The left column. (**a**) Loop 3 of cardiac myosin (PDB 7JH7, (Risi et al. 2021a)) does not interact with actin, because it is pulled toward the body of myosin (plum) by a pair of internal salt bridges (blue circles and blue squares connected with black lines). (**b**) Loop 3 of myosin IIC (PDB 5JLH; (von der Ecken et al. 2016)) forms charged interactions with SD1 of the lower actin subunit (blue circles). (**c**) Loop 3 of myosin VI (PDB 6BNP; (Gurel et al. 2017)) electrostatically interacts with SD1 (blue squares) and SD2 (blue triangles) of the lower actin subunit. A salt bridge with SD1 is formed during the Strong ADP to Rigor transition (blue stars). (**d**) Loop 3 of myosin Ib (PDB 6C1H; (Mentes et al. 2018)) forms electrostatic interactions (purple circles) and hydrogen bonds (brown circles and squares) with actin's SD1

The transition from the weakly bound myosin to higher affinity actomyosin complexes (e.g., strong ADP and rigor) involves a rotation of the U50 that closes the actin-binding cleft. This U50 movement brings the CM loop (Fig. 14.9a, blue) into position to form several key interactions characteristic to the rigor state. The class II myosins exhibit very similar interfaces of their CM loops with actin, primarily governed by a trio of hydrophobic residues on the antiparallel β-sheets (Fig. 14.12a–b, purple circles). Additional stabilization at the base of the CM loop is provided by electrostatic contact of a conserved lysine residue with a pair of negatively charged residues at the junction of SD1 and SD3 (Fig. 14.12a–b, blue circles). Myosin IIC contains an isoform-specific salt bridge at the CM loop tip, which associates with the region near the SD1–SD2 junction (Fig. 14.12b, blue squares). The myosin VI CM loop possesses a nearly identical actin footprint to the class II myosins, despite the difference in the specific contacts that form this

interface. The hydrophobic interactions are clustered at the tip of the loop (Fig. 14.12c, purple circles), while an electrostatic interaction also exists in the base but on the opposite strand (Fig. 14.12c, blue circles). In contrast to the multiple interactions sustaining these CM loop interfaces, a single glutamic acid of myosin Ib is responsible for its CM loop interaction with a nucleotide-coordinating lysine residue of actin (Fig. 14.12d, blue circles). This CM loop residue also serves as a phosphorylation site important for the activation of class I myosins (Bement and Mooseker 1995).

Loop 2, the HTH motif, and the CM loop are the three myosin surface elements that form the core of its actin interface, which spans across the actin filament's longitudinal interface. Auxiliary contributions to this core footprint come from loop 4 (Fig. 14.9a, yellow) of the U50 and loop 3 (Fig. 14.9a, orange) of the L50. In the case of loop 4, minimal variability is observed among the actin interfaces of each isoform. For class II myosins, a conserved acidic residue at its tip mediates electrostatic interaction with positively charged actin side chains (Fig. 14.13a, b, blue circles). Furthermore, an arginine residue in both cardiac myosin and myosin IIC (Fig. 14.13a, b, blue squares) forms charged interactions with the tropomyosin (Tm) cable (Fig. 14.9a, black), which blankets the actin filament in numerous cell types and regulates the availability of myosin's binding sites on actin. For myosin VI, an acidic residue located closer to the loop 4 base interacts with the same basic residue on actin as the class II myosins (Fig. 14.13c, blue circles). The tip of myosin Ib loop 4 interacts with the same zone on actin as observed for class II myosins; however, these contacts are hydrophobic rather than electrostatic (Fig. 14.13d, purple circles).

Unlike the relative conservation displayed by loop 4, myosin isoforms demonstrate great variability in their loop 3 actin interfaces. Loop 3 represents the only actin-binding element that does not interact with the upper actin subunit. For myosin IIC, a pair of basic residues interacts with the negatively charged "Milligan contact" (Fig. 14.14b, blue circles) (Milligan 1996). A different set of charged residues on myosin VI forms electrostatic contacts with a distinct zone on actin that includes the D-loop (Fig. 14.14c, blue squares and triangles). Furthermore, one of these interactions (Fig. 14.14c, blue stars) is formed upon the transition from strong ADP to rigor (Gurel et al. 2017). In contrast to the salt bridges maintaining the loop 3 actin interfaces of myosins IIC and VI, myosin Ib exhibits an assortment of hydrophobic interactions (Fig. 14.14d, purple circles) and H-bonds (Fig. 14.14d, brown circles and squares) with a region just above the Milligan contact. Loop 3 of cardiac myosin represents a dramatic departure from the other isoforms since it does not appear to interact with actin in the rigor state. Instead, a pair of salt bridges between loop 3 and the body of cardiac myosin (Fig. 14.14a, blue circles and squares) keeps it sequestered from the actin interface.

Variations in the Actin-Binding Elements of Various Myosin Isoforms Tune Up Their Kinetic Parameters

A generally conserved blueprint with isoform-specific details maintains the strong actin-binding states of the cross-bridge cycle. The variant sequences and structures of these actin-binding elements between myosin classes contribute to their kinetic properties, as evidenced by altered ATPase cycle kinetics upon chimeric replacement of loop 2 (Uyeda et al. 1994). Thus, these modifications are a source of kinetic fine-tuning during the interaction of myosin motors with a highly conserved actin track, which in turn biases myosin isoforms for certain biological functions (Robert-Paganin et al. 2020; Spudich 1994). Since the strong ADP and rigor actin-binding interfaces are similar, differences in the transducer (Clark et al. 2005; Sweeney et al. 1998) and lever arm (Mentes et al. 2018) are likely the most important for tuning the ADP release step. By contrast, the duration of actin attachment (i.e., duty ratio) and the sliding velocity can be modulated by variant details of the common actin-binding architecture (Robert-Paganin et al. 2020).

The set of isoforms for which high-resolution rigor actomyosin complexes are available represents a mixture of kinetically and functionally diverse myosins, which can be divided into broad groupings based on the parameters of their cross-bridge cycles (reviewed in (Bloemink and Geeves 2011)). The class II myosins serve contractile functions within cells by aggregating into filaments (Fig. 14.4c). However, cardiac myosin moves actin filaments at a velocity that is over an order of magnitude greater than that of myosin IIC (Heissler et al. 2013; Yamashita et al. 1994). While the HTH motif (Fig. 14.11a, b), CM loop (Fig. 14.12a, b), and loop 4 (Fig. 14.13a, b) exhibit largely similar actin interfaces between these two isoforms, significant variability can be observed with respect to loops 2 (Fig. 14.10a, b) and 3 (Fig. 14.14a, b). The reduced interactivity of these elements in cardiac myosin, compared with myosin IIC, would be beneficial for the rapid attachment and detachment of myosin head ensembles. Thus, these differences in the actin-binding interface may contribute to its greater sliding velocity and lower duty ratio. In contrast to this mechanism which depends on short-lived Rigor interactions, the processive myosin VI motor depends on persistent actin attachment of its dimerized heads for its cargo-transporting function (Fig. 14.4d). Accordingly, its duty ratio of 0.9 (i.e., spends 90% of the cross-bridge cycle bound to actin) is among the highest observed in the entire myosin superfamily (De La Cruz et al. 2001; Robblee et al. 2004). Out of all the characterized rigor actomyosin complexes, loop 3 of myosin VI (Fig. 14.14c) possesses the most extensive contacts with the lower actin subunit. This could play a part in the stability of its strong binding to actin, an important component of its processive mechanism in which at least one myosin head is bound to actin at all times (Sweeney et al. 2007). Finally, myosin Ib represents the strain-sensing class I myosins, which can anchor themselves between the actin cytoskeleton and the cell membrane for extended periods in response to mechanical loads (Fig. 14.4b). Myosin Ib dynamically adjusts to an imposed tension by increasing its actin attachment lifetime, such that it transitions from a low (0.2) to high (0.9) duty

ratio motor (Laakso et al. 2008). Despite its ability to prolong its actin attachment in response to force, the rigor interface of myosin Ib is notably diminished compared to other isoforms. This is especially true for the CM loop and HTH motif, both integral components of the core interface. Thus, kinetic tuning of myosin Ib for its force-sensing cellular role is likely controlled by elements outside the actin-binding interface, such as its N-terminal extension near the motor domain-lever arm interface (Fig. 14.8a–e, pink) (Mentes et al. 2018; Shuman et al. 2014).

Cellular and Physiological Contexts of Actomyosin Interaction

Muscle Contraction

Although muscle contraction is the biological process typically associated with the actomyosin interactions, it represents a late evolutionary arrival to the functional repertoire of interaction between actin and myosin. Myosin participates in cargo transport and cytoskeletal dynamics in nearly all eukaryotes, and it was adapted for powering large-scale motility of metazoans upon the origin of functional muscle tissue. Striated (i.e., skeletal and cardiac) and smooth muscles differ with respect to the assembly of their contractile apparatuses as well as the regulatory mechanisms governing their contractions. The characteristic functional unit of a striated muscle fiber is the sarcomere, whose lateral boundaries are formed by the Z-lines that anchor myosin-based thick filaments and actin-based thin filaments (Fig. 14.15a). During striated muscle contraction, the thin filaments are pulled toward the M-line at the sarcomere's center by the formation and detachment of myosin cross-bridges, which consequently reduces the distance between the two Z-lines (Fig. 14.15b). Thus, the molecular basis of striated muscle contraction consists of sarcomeric shortening as the thick and thin filaments slide past each other (Huxley and Hanson 1954). This sliding motion of thick and thin filaments also occurs in the smooth muscle cells found in blood vessels, airways, and the gut. However, their contractile apparatus is not a tightly ordered sarcomere but rather a more flexible lattice of thin filaments and variable-length thick filaments (Liu et al. 2013) interconnected by dense bodies which are functionally equivalent to the Z-disks of striated muscle (Herrera et al. 2005; Zhang et al. 2010).

A functional property mutual to both striated and smooth muscle is their force-velocity (F-V) relationship (Fig. 14.15c), which entails that resistive load applied to muscle decreases its shortening velocity (Hill 1938). For forces greater than the isometric stall force at which no net movement of actin occurs (Fmax), the system reproduced the negative velocity that defines eccentric muscular contraction (Debold et al. 2005). Single-molecule analysis of cardiac actomyosin cross-bridges reveals load dependence of ADP release, and this parallels the inverse relationship between cardiac contractile velocity and external load (Sung et al. 2015). However, the

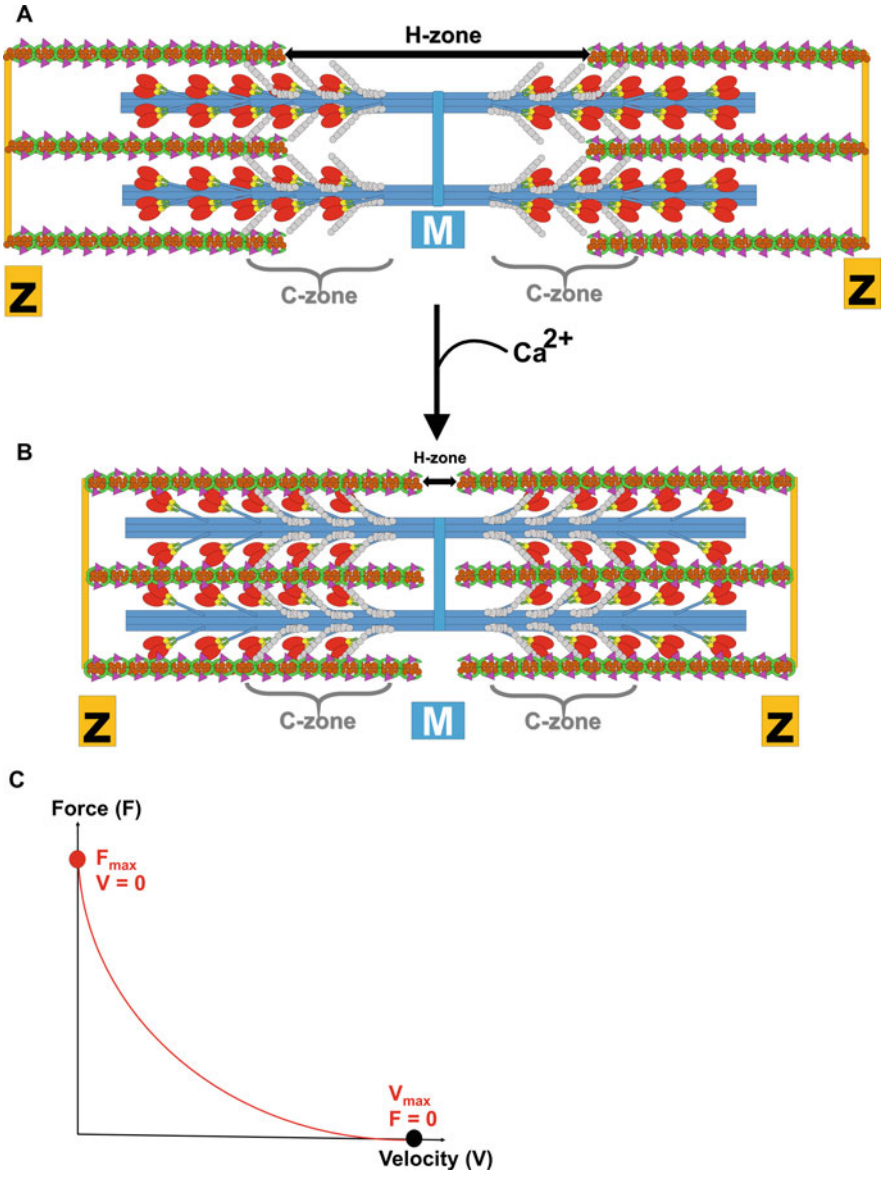

Fig. 14.15 Structural and functional properties of the striated muscle sarcomere. (**a, b**) Schematic view of sarcomeric relaxation and contraction, a physiological process driven by interactions between actin-based thin filaments (brown circles) and myosin-based thick filaments (blue rectangles). The myosin heads are red ovals. The calcium-sensing troponin complex (pink) and tropomyosin cable (green) associated with the actin filaments regulate binding of myosin. Thin filaments are anchored on both sides by the Z-lines (gold rectangles), which form the lateral boundaries of a single sarcomeric unit. Myosin-binding protein C (gray), located within the sarcomeric C-zones (gray brackets), interacts with both thick and thin filaments. (**a**) Sarcomere in its relaxed (i.e., lengthened) state has its Z-lines distanced from each other such that a large gap between the thin

degree of coupling between load and ADP release for β-cardiac myosin (ventricular isoform) is far less than that of myosin V (Veigel et al. 2005) or myosin Ib (Laakso et al. 2008), and this likely contributes to cardiac muscle's efficient systolic power output against the resistance of ventricular filling (Greenberg et al. 2014). Compared to striated muscle, smooth muscle exhibits one-tenth the maximum shortening velocity (Vmax) (Warshaw et al. 1990) and three- to fourfold greater force development under maximal load (Harris et al. 1994). The higher duty ratio of smooth muscle myosin is the biochemical basis of these mechanical differences (Guilford et al. 1997). In tissues with a mixture of different muscle myosin isoforms, the cross-bridges of the slower isoform limit the velocity of the faster ones by exerting a load on them (Warshaw et al. 1990).

In addition to variations in the contractile apparatus structure and F-V relationship, smooth and striated muscles also differ with respect to their functional regulatory mechanisms. Smooth muscle activation is achieved by phosphorylation of Ser19 within its RLC by a smooth muscle-specific myosin light chain kinase (Pearson et al. 1984) (Fig. 14.4h). RLC phosphorylation triggers relaxed myosin heads in the "off" state (i.e., interacting heads motif or IHM configuration) to release from the thick filament backbone and become available for cross-bridge formation. RLC phosphorylation can also release striated muscle myosins from the relaxed IHM state (Zhao et al. 2009). However, due to an additional regulatory layer contained in skeletal and cardiac thin filaments, RLC phosphorylation only serves a modulatory role. In striated muscle, the accessibility of myosin's binding sites on actin filaments is controlled by Ca^{2+} binding to the tropomyosin-troponin complex (Drabikowski et al. 1968; Ebashi 1972; Lehrer and Morris 1982; Martyn et al. 2001). Together, actin and its regulatory apparatus are referred to as the thin filament (Fig. 14.16a, b). The tropomyosin (Tm) cable is a double-stranded α-helical coiled-coil that wraps around actin filaments (Fig. 14.16a, b, blue ribbons) in a diverse array of cell types (Brown et al. 2001; Parry 1975). The Tm cable is associated with the calcium-sensing troponin complex (Fig. 14.16a, b, green, red, and purple ribbons) spaced at intervals of every seven actin subunits. Early kinetic experiments established that Tm sterically blocks actomyosin interactions in the absence of Ca^{2+}, whereas the presence of Ca^{2+} increases the proportion of activated thin filaments capable of binding myosin (McKillop and Geeves 1993).

Recent cryo-EM studies of both native and reconstituted cardiac thin filaments have clarified the molecular details of Ca^{2+}-mediated thin filament regulation (Risi

Fig. 14.15 (continued) filament ends (H-zone) is visible (black double-sided arrow). (**b**) Sarcomere in its contracted (i.e., shortened) state has thin filaments translocated toward the sarcomere's midline (M-line; blue rectangle), which reduces the length of the H-zone (black double-sided arrow). (**c**) Hyperbolic relationship between the force and velocity of muscular contraction. The red circle located at the y-intercept (Fmax) represents the "stall force" at which sarcomere length remains fixed and the sliding velocity of the thin filaments is equal to zero. The black circle located at the x-intercept (Vmax) represents the maximum shortening velocity of the sarcomere, which can be reached when the force applied to it equals zero

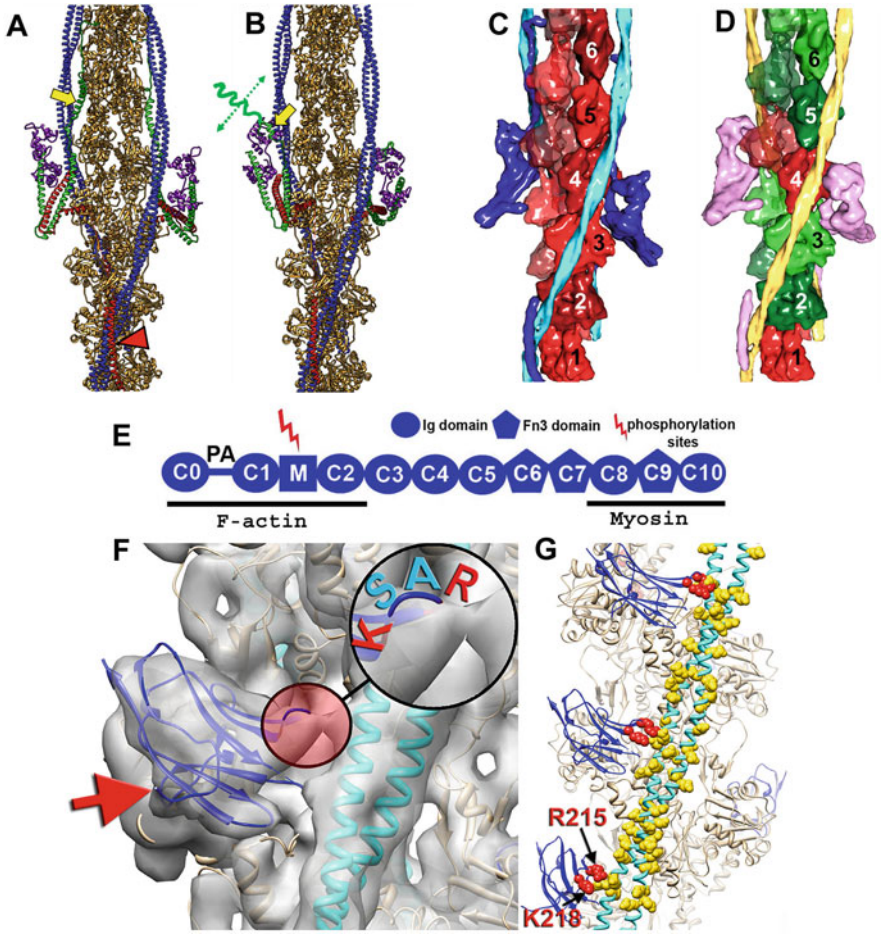

Fig. 14.16 Regulatory components of the cardiac sarcomere. (**a, b**) Conformational changes of the troponin-tropomyosin complex during the transition from Ca^{2+}-free state (PDB 7KO4; (Risi et al. 2021a)) to Ca^{2+}-bound state (PDB 7KO5; (Risi et al. 2021a)). The actin subunits are tan, while Tm cable is blue. The regulatory Tn complex consists of three subunits—Ca^{2+}-binding TnC (purple), Tm-binding TnT (red), and inhibitive TnI (green). The N-terminal helix of TnT binds to the junction region between the two adjacent Tm molecules across the actin strand to stabilize it (red arrowhead). (**a**) At low Ca^{2+} levels, the C-terminal region of troponin I (green) is tightly bound to actin (tan) and Tm (blue), as indicated by the yellow arrow. The Ca^{2+}-binding TnC (purple) is in its closed conformation. The Tm cable (blue) is positioned such that each individual actin-binding site is inaccessible to myosin. (**b**) Upon Ca^{2+} binding, the cleft of TnC opens and TnI "regulatory switch" helix dissociates from actin and Tm and binds to TnC (yellow arrow). The rest of the TnI C-terminus becomes disordered (green dashed arrow). This conformational change unlocks the Tm cable so that it can move azimuthally to expose the myosin-binding sites on actin. (**c–d**) Azimuthal rotation of Tm cable upon binding of Ca^{2+} to TnC exposes myosin-binding sites on actin. (**c**) At low Ca^{2+} levels actin subunits (shown in red) have their myosin binding site sterically blocked by the Tm cable (light blue). (**d**) At activating Ca^{2+} levels due to azimuthal movement of Tm (yellow) four out of six actin subunits have their myosin binding sites exposed (shown in

et al. 2021b; Yamada et al. 2020). Structural changes of troponin (Tn) mechanistically link Ca^{2+} levels with the position of the Tm cable. When a Ca^{2+} ion binds to the TnC subunit (Fig. 14.16a and b, purple), the C-terminal part of the TnI subunit (Fig. 14.16a and b, green) releases from the actin filament (Fig. 14.16b, green dotted arrow) and its "regulatory switch" helix binds TnC cleft that was opened by a Ca^{2+} ion (Fig. 14.16b, yellow arrow). This conformational change liberates the Tm cable (Fig. 14.16a and b, blue) so that it can azimuthally rotate along with the N-terminal portion of TnT (Fig. 14.16a red arrowhead) in order to permit actomyosin interactions (Risi et al. 2021b; Yamada et al. 2020). At low Ca^{2+} levels, the positioning of Tm on actin subunits sterically hinders myosin from binding to its interaction sites on the actin filament (Fig. 14.16c). At permissive Ca^{2+} concentrations, the Tm rolls away from the myosin binding sites on four out of six actins so that those actin subunits are accessible to myosin binding (Fig. 14.16d) (Risi et al. 2021b; Yamada et al. 2020). A recent cryo-EM study of the native cardiac thin filament at systolic Ca^{2+} concentration revealed a primarily stochastic binding of Ca^{2+} ions to the Tn complex along the thin filament (Risi et al. 2021b). This suggests that during the systolic phase of the heartbeat, the Ca^{2+} influx randomly activates sections of the thin filament, providing myosin heads with equal opportunity to bind at various locations. Both myosin RLC phosphorylation and Ca^{2+}-mediated thin filament activation have distinct regulatory contributions to a property of cardiac muscle known as length-dependent activation (LDA). Also known as the Frank-Starling law, the principle of LDA states that with increased length, cardiac myofilaments exhibit greater force development and calcium sensitivity (Allen and Kentish 1985; Dobesh et al. 2002). Upon cardiac sarcomere stretching, liberation of myosin heads from their folded-back conformation on the thick filament underlies elevated force development, whereas increased Ca^{2+} sensitivity derives from structural changes to the regulatory Tn complex of the thin filament (Zhang et al. 2017).

Myosin-binding protein C (MyBP-C) (Fig. 14.16e) represents another striated muscle-specific regulatory layer for managing the actomyosin interaction. This

Fig. 14.16 (continued) green). The two actin subunits remain unavailable for actomyosin interactions (shown in red) due to steric blocking by the N-terminus of TnT (subunit 1) or the core of Tn complex (subunit 4). (**e**) The domain composition of the cardiac myosin binding protein C (cMyBP-C). Skeletal MyBP-C isoforms contain seven immunoglobulin (Ig)-like domains, three fibronectin (Fn)-like domains, and a regulatory M-domain between the C1 and C2 Ig-domains, which carry regulatory phosphorylation sites (red arrow). Cardiac isoform of MyBP-C has an additional Ig-domain (e.g., C0) at its N-terminus connected to C1 via proline/alanine (PA) linker. N-terminal C0, C1, M, and C2 domains bind to actin containing thin filament, while C-terminal C8, C9 and C10 domains keep MyBP-C attached to the myosin thick filament. (**f**) Cryo-EM map (gray transparent surface) shows that C1 Ig domain of cMyBP-C (blue ribbons) binds to actin subunit (tan ribbons, contact marked with red arrow) and cross-links it with the Tm cable (cyan ribbons) via its positively charged loop (red circle), which moves Tm cable into fully activated position. (**g**) Interactions of positively charged residues R215 and K218 of cMyBP-C C1 Ig domain (red spheres) occur *via* formation of salt bridges with the negatively charged patches (yellow spheres) on the Tm cable (PDB 6G2T; (Risi et al. 2018)). Actin is tan, while C1 Ig domain is blue. Activated Tm cable is cyan

unique protein comprised of ten domains (Fig. 14.16e) cross-links thin and thick filamentous systems in the sarcomere (Luther et al. 2011). The consensus from studies of the cardiac form of MyBP-C establishes that while it is not essential for assembly and stability of the sarcomere (Harris et al. 2002), its interactions with both thin and thick filaments modulate the rate and force of cardiac contractions (reviewed in (Moss et al. 2015)). Depending on the sarcomeric calcium level, cMyBP-C appears to possess dual functionality with respect to cross-bridge modulation. At low calcium, cMyBP-C enhances the activation of the thin filament (Previs et al. 2015; Razumova et al. 2008; Razumova et al. 2006) and myosin binding (Inchingolo et al. 2019). The structural basis for enhanced thin filament activation presumably derives from an electrostatic interaction between the C1 domain in the cMyBP-C N-terminal region and the Tm cable, which activates cardiac thin filaments (Fig. 14.16f and g) (Risi et al. 2018). At high Ca^{2+}, the role of cMyBP-C transforms into inhibition of cross-bridge formation and sliding velocity, as it binds in clusters to the thin filament and thus blocks myosin's access to its binding sites (Inchingolo et al. 2019; Previs et al. 2016). Much like sarcomeric Ca^{2+} concentration, phosphorylation of MyBP-C exerts regulatory control over actomyosin cross-bridges. Phosphorylation of MyBP-C M-domain relieves MyBP-C binding to the S2 region of inactive myosin heads (Gruen et al. 1999) and is an important part of contractile regulation (Nag et al. 2017). High Ca^{2+} is required for the phosphorylated MyBP-C to activate the thin filament (Colson et al. 2016; Previs et al. 2016).

Cargo Transport

In contrast to the ensemble of low-duty ratio myosin motors responsible for muscle contraction, cargo motility along actin filaments utilizes higher-duty ratio processive myosins that can fulfill their biological function as a single monomer or dimer. Myosin X (Fig. 14.17a, labeled (1)), which moves in large side steps along actin bundles, transports cargoes with important functional roles in nervous system development. Spatial patterning of the embryonic nervous system depends on morphogen gradients, transmitted between cells by specialized actin bundles known as cytonemes (Kornberg and Roy 2014). Myosin X motility along these bundles enables the transport of the morphogens Sonic hedgehog (Shh) in chick embryos (Sanders et al. 2013) and Wnt in zebrafish embryos (Stanganello et al. 2015) (Fig. 14.17b). Consistently, mice with myosin X knocked out exhibit alterations to the Shh gradient within the embryonic neural tube (Hall et al. 2021). Myosin-based cargo transport can also regulate synaptic plasticity in the adult nervous system. Myosin V (Fig. 14.17a, labeled (2)) travels on F-actin from the minus to the plus end (Fig. 14.17c, black arrow). It delivers AMPA glutamate receptors from the cytosol to the dendritic spines in hippocampal neurons, thus facilitating long-term potentiation (LTP) (Fig. 14.17c) (Correia et al. 2008). Whereas LTP enhances synaptic connectivity, its opposing process known as long-term depression (LTD) reduces synaptic connectivity. The myosin VI motor

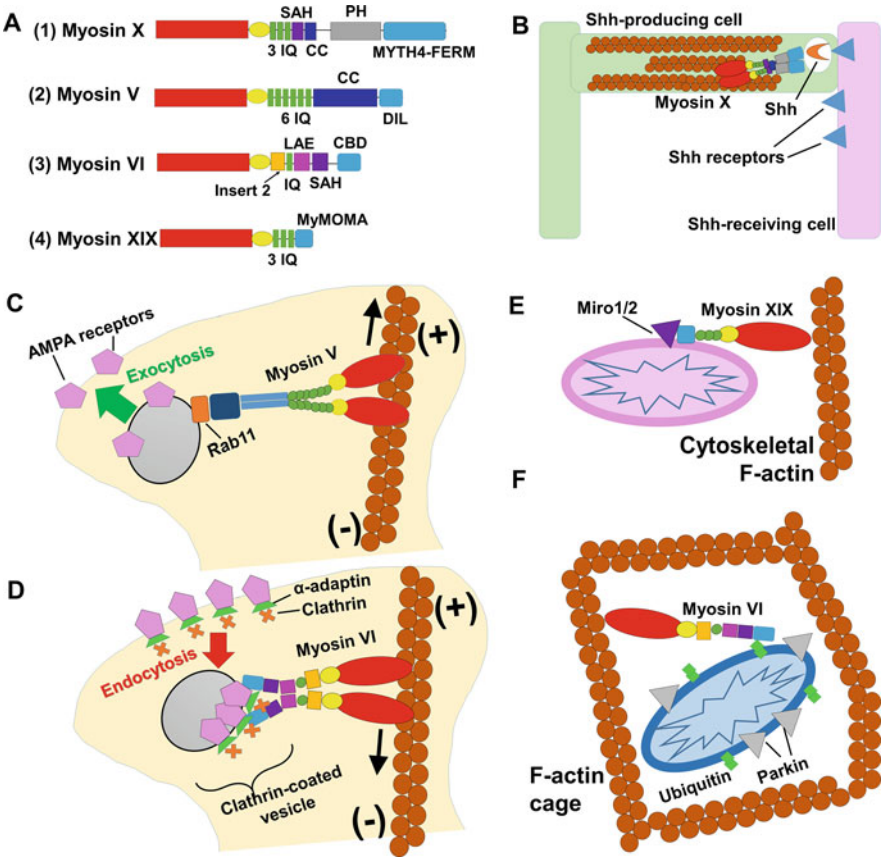

Fig. 14.17 Structure and function of various cargo-transporting myosin classes. (**a**) Domain architecture of various cargo-transporting myosin classes. While these isoforms all have a conserved motor (red rectangles) and converter (yellow ovals) domains, they differ in their tail domain architecture that follows the converter. The cargo-binding domains (light blue rectangles) residing in myosin isoforms tails possess different structures and determine cargo specificities. (1) Myosin X contains 3 IQ motifs (green), a single alpha helix (SAH; purple), a coiled-coil (CC; blue) domain that allows antiparallel dimerization, membrane-binding pleckstrin homology domain (PH; gray), and a cargo-binding MyTH4-FERM domain (light blue). (2) Myosin V contains 6 IQ motifs (green), a coiled-coil domain (CC; blue) responsible for dimerization, and a dilute (DIL; light blue) domain that provides cargo binding. (3) Myosin VI contains a unique 'insert 2' immediately after the converter (orange) that confers its reverse (i.e. minus-end) directionality, one IQ motif (green), a lever arm extension (LAE; magenta), single alpha helix (SAH; purple), and a cargo-binding domain (CBD; light blue). (4) Myosin XIX contains 3 IQ motifs (green) and a MYO19-specific mitochondrial outer membrane association (MyMOMA; light blue) tail domain. (**b**) Myosin X forms a dimer to transport vesicles (while oval) containing sonic hedgehog (Shh; orange crescent) along actin bundles known as cytonemes (brown). These bundles project from the Shh-producing cell (light green) to the Shh-receiving cell (light pink), which allows the Shh ligand to be directly delivered to its target receptor (blue triangles) by myosin X-mediated transport. (**c**) As a result of LTP-inducing stimuli to a postsynaptic neuron (tan), myosin V dimers bind to the Rab11 adaptor protein (orange rectangle) on the surface of a recycling endosome (gray oval) containing AMPA receptors (pink pentagons). This facilitates the endocytic trafficking (green arrow) of AMPA

(Fig. 14.17a, labeled (3)), which exhibits unique directionality toward the minus end of actin (Fig. 14.17d, black arrow), is well-suited to carry out LTD. It can transport AMPA receptors from the membrane (plus end) to the neuron interior (minus end) via clathrin-mediated endocytosis (Fig. 14.17d) (Wagner et al. 2019).

Myosin motors also move entire organelles along the actin cytoskeleton. The metazoan-specific myosin XIX (Fig. 14.17a, labeled (4)) is engineered for mitochondrial transport, as its tail domain contains specific elements that recruit it to these organelles (Fig. 14.17e) (Quintero et al. 2009). These features include a lipid-binding motif that targets the outer mitochondrial membrane (Fig. 14.17e, pink oval) (Hawthorne et al. 2016) and a region which specifies binding to the mitochondrial surface proteins Miro1/2 (Fig. 14.17e, purple triangle) (Oeding et al. 2018). Myosin XIX-driven mitochondrial motility is essential for proper execution of mitosis, as it ensures the delivery of an equal number of organelles to each daughter cell (Rohn et al. 2014). While myosin XIX handles the transport of healthy functional mitochondria (Fig. 14.17e), myosin VI has been found to interact with dysfunctional mitochondria and regulate a key quality control pathway. Damaged mitochondria (Fig. 14.17f, blue ovals) express the ubiquitin ligase parkin (Fig. 14.17f, gray triangles) on their outer membrane. Parkin tags the outer mitochondrial membrane proteins with ubiquitin (green diamonds), which in turn acts as a recruitment signal for myosin VI to bind and deposit the organelles within assembled F-actin cages (Fig. 14.17f, brown), effectively isolating them from the internal cellular environment (Kruppa et al. 2018). The well-studied processive myosin V motor has also several organelle transport functions characterized in a variety of eukaryotes. Delivery of organelle cargoes to the budding daughter cells in yeast depends on their binding to specific adaptor proteins which can be recognized by the class myosin V tail. Different adaptors facilitate myosin V-mediated transport of vacuoles (Ishikawa et al. 2003), peroxisomes (Fagarasanu et al. 2006), and trans-Golgi vesicles (Lipatova et al. 2008). Since yeast class V myosins are less processive than their vertebrate counterparts (Reck-Peterson et al. 2001), multiple myosin V motors are required to rapidly transport cargo to active growth sites in yeast (Donovan and Bretscher 2012). In vertebrates, class V myosins transport organelles in a multitude of physiological contexts, from the melanosomes involved in skin and hair

Fig. 14.17 (continued) receptors to the post-synaptic membrane due to processive movement of Myosin V toward the plus end of F-actin (black arrow). (**d**) Myosin VI dimers form a complex with AMPA receptors (pink pentagons) and α-adaptin (green trapezoids) and move them toward the minus end of F-actin (black arrow). This facilitates endocytosis (red arrow) of the AMPA receptors into clathrin (orange crosses)-coated vesicles (gray ovals), and in doing so promotes synaptic LTD. (**e**) The MyMOMA tail domain of myosin XIX binds to both the mitochondrial outer membrane (pink oval) and the mitochondrial surface proteins Miro1/2 (purple triangle), allowing it to transport healthy organelles along cytoskeletal F-actin tracks (brown). (**f**) The outer membrane of damaged mitochondria (blue oval) accumulates parkin (gray triangles), which tags the outer mitochondrial membrane proteins with ubiquitin (green diamonds). Myosin VI binds to the ubiquitin and triggers the assembly of an F-actin cage (brown) that sequesters the dysfunctional organelle

pigmentation (Wu et al. 2002) to the endoplasmic reticulum in cerebellar neurons that mediates synaptic plasticity (Wagner et al. 2011).

Tension Sensing

The regulation of plasma membrane tension is essential for proper cellular function, as it links mechanical stimuli to biochemical responses. Class I myosins are poised to act as tension sensors due to their conserved TH1 tail domains, which can bind phospholipids and thus link the plasma membrane to the internal cytoskeleton bound by the motor domain (reviewed in (McConnell and Tyska 2010)). The total tension of the plasma membrane is largely determined by the molecular interfaces, such as myosins, that adhere it to the cytoskeleton (Sheetz 2001). Myosin Ia supports biomechanical interaction between membrane and cytoskeleton in the brush border of intestinal epithelial cells (Nambiar et al. 2009). Loss of myosin Ia destabilizes the brush border architecture (Tyska et al. 2005).

The extreme tension sensitivity of myosin Ib (Fig. 14.18a) allows it to facilitate the extension of membrane tubules at endosomes and the trans-Golgi network (Laakso et al. 2008). As this process involves an increase in membrane tension, the catch-bond behavior of myosin Ib allows it to remain attached to the tubule while elongating it at a constant velocity along an actin filament (Fig. 14.18b) (Yamada et al. 2014). The force sensitivity of myosin Ib is dramatically abrogated in the presence of Ca^{2+}. It accelerates myosin Ib detachment from actin at 1 pN of force by 19-fold, due to reduction of the working stroke distance required to induce ADP release (Lewis et al. 2012). The less force-sensitive myosin Ic (Greenberg et al. 2012) also has the lifetime of its detached state increased by Ca^{2+} addition, though in this case Ca^{2+} exerts its effect primarily via deceleration of ATP hydrolysis (Adamek et al. 2008). The response of myosin Ic to Ca^{2+}suits it for its biological role in sensory adaptation within the inner ear's hair cells, a process intimately dependent on calcium transients. Myosin Ic links the transduction channels through which Ca^{2+} ions pass to the actin bundles within the hair cells known as stereocilia. An extracellular tip link connects the ion channel associated with one stereocilia bundle to its neighboring bundle. Auditory stimuli increase tension in the tip links and leads to subsequent Ca^{2+} influx through the transduction channels. The myosin Ic-transduction channel complex dynamically adjusts to tip link tension and elevated calcium by undergoing displacement along the stereocilia to restore resting tension levels (Batters et al. 2004; Holt et al. 2002). Thus, dual Ca^{2+} and tension sensitivity of myosin Ic allows it to mechanically transduce stimuli applied to the hair cells.

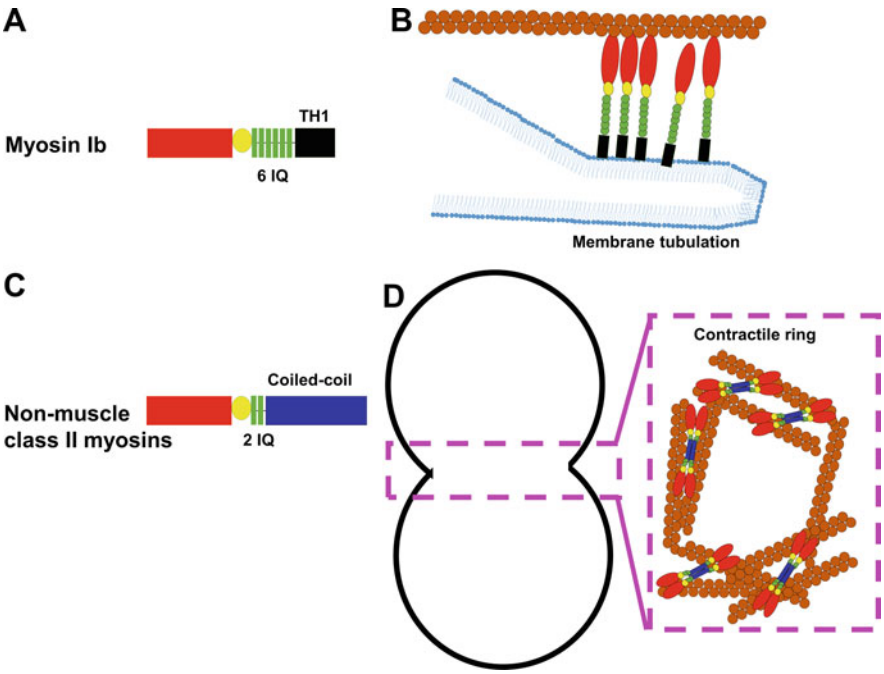

Fig. 14.18 Involvement of myosins in tension sensing and cytoskeletal remodeling. (**a**) Myosin Ib, is comprised of a motor domain (red rectangle), converter (yellow circle), 6 IQ motifs in the lever arm (green rectangles), and a membrane-binding TH1 domain (black rectangle). (**b**) Participation of tension-sensing myosin Ib monomers in the extension of membrane tubules. In response to an increase in tension of the cell membrane (blue) during tubulation, myosin Ib motors adopt a long-lived state of cross-bridge formation with actin filaments (brown). This catch-bond behavior allows myosin Ib to facilitate tubule elongation while remaining anchored to the cytoskeleton. (**c**) Non-muscle class II myosins are comprised of a motor domain (red rectangle), converter (yellow circle), 2 IQ motifs in the lever arm (green rectangles), and a coiled-coil domain (blue rectangle) that mediates dimerization. (**d**) Participation of non-muscle class II myosins in the formation of the cleavage furrow (magenta dashed rectangle) during cytokinesis. A ring of actin filaments (brown) is assembled at the center of the dividing cell (black outline). The contractile force exerted by short bipolar myosin II filaments tightens the ring, resulting in the cleavage furrow that drives cytokinesis

Cytoskeletal Remodeling and Motility

Motility of single cell eukaryotes via actin cytoskeleton remodeling was one of the primordial functions of the non-muscle class II myosins (Fig. 14.18c), and it has been adopted by numerous motile cell types within complex multicellular eukaryotes. Cellular locomotion consists of two distinct phases, differentiated by the relative involvement of actin and myosin (Chen 1981; Lauffenburger and Horwitz 1996). The first phase involves extension of the cell's leading edge, and this is mainly determined by actin polymerization dynamics independent of myosin (Fig. 14.2b–d). Accordingly, leading edge extension is not affected by myosin null

mutations in *Dictyostelium* (Wessels et al. 1991). Once the membrane protrusion has adhered to the cellular substratum, myosin-mediated contractility behind the leading edge generates the force needed to propel the cell body forward. In the amoeboid *Dictyostelium*, myosin II undergoes dynamic polarized redistribution to the rear of a cell moving toward a chemotactic stimulus (Yumura 1996). This same model organism also demonstrates that during cytokinesis (Fig. 14.18d), myosin localizes to the contractile ring at the cell equator in order to promote daughter cell segregation. Studies of this phenomenon in mammalian cells reveals that the non-muscle class II myosins contain motifs within their tails that mediate recruitment to the cleavage furrow as well as incorporation into preexisting myosin II filaments at the furrow (Beach and Egelhoff 2009). Parallels between amoebal and mammalian cytoskeletal dynamics can also be observed in motile immune cells. The T-cell class of lymphocytes depends on migration through the vascular endothelial wall in order to reach infected tissues and exert its effect or functions. As in *Dictyostelium*, leading edge extension occurs independently of myosin activity, given that T cells lacking myosin IIA can squeeze their membrane protrusions through the endothelial barrier. However, myosin IIA contractile activity is required for complete extravasation of the T cell through the endothelium (Jacobelli et al. 2013).

Conclusion and Future Perspectives

The actomyosin interaction originated in unicellular eukaryotes as a mechanism governing motility at the cellular scale, and the emergence of eukaryotic complexity coincided with functional diversification of the myosin superfamily. Consequently, myosin plays a functional role in nearly all tissues of a typical multicellular eukaryote. The structural features of each myosin class were adapted to their distinct cellular duties (Fig. 14.4b–e and Figs. 14.17 and 14.18), which form the molecular basis of diverse physiological processes such as nervous system development, intestinal absorption, and immune cell migration. Thus, eukaryotic evolution generated a protein family with a conserved structural blueprint and kinetic cycle. Fine-tuning was accomplished via sequence divergence of certain motifs, which altered the rate and equilibrium constants of the ATPase cycle (reviewed in (De La Cruz and Ostap 2004)). Consequently, the myosin superfamily members possess variations in their actin sliding velocities by a factor of 300 and in actin-activated ATPase activity by a factor of 3000, despite the general conservation of the motor domain architecture responsible for actin binding and ATP hydrolysis (Heissler and Sellers 2016).

Myosin is a catalytic molecular machine governed by allosteric communication between three major regions: the actin-binding interface, nucleotide-binding pocket, and force-generating lever arm (Figs. 14.5, 14.6, and 14.7). Thus, isoform-specific changes in any of these regions tune up the overall functionality of the myosin enzyme to a particular cellular task. For example, a class XI myosin from the algal species *Chara corallina* possesses a unique charge distribution of actin-binding

loops 2 and 3 and as a result exhibits an exceptionally fast velocity ten times greater than that of fast skeletal muscle myosin (Ito et al. 2007). Despite sharing a similar general mechanism of processively translocating actin filaments, myosins from classes V, VI, and X have distinct lever arm and tail domain architectures (Fig. 14.17). This diversity endows processive myosins with varied step sizes and directionality, with parallel variability in their motor domains and mechanochemical cycle parameters. The reverse directionality of myosin VI, conferred by a class-specific lever arm insert, necessitates a different gating mechanism for its lead head than myosin V. Gating of myosin VI processivity relies on another unique insert, located in its motor domain near the nucleotide-binding site (Sweeney et al. 2007). In the case of myosin X, its tail architecture is the primary reason behind its selectivity for actin bundles, although chimeric replacement of its motor domain with that of myosin V reveals that the head also confers some of this behavior (Nagy et al. 2010). The extensive menagerie of myosin motors is punctuated by remarkable feats of conservation such as the IHM state of muscle myosin autoinhibition, governed by residues that have largely resisted variation for nearly 800 Myrs of metazoan evolution (Alamo et al. 2016). This regulatory mechanism dates back to the primitive muscular system of jellyfish (Lee et al. 2018).

Molecular disparities among myosins are largely responsible for the varied actomyosin interactions in physiological contexts, as the evolution of the actin superfamily has proceeded along a much less divergent trajectory. The exceptional conservation of actin is apparent when comparing evolutionarily distant eukaryotic species, given the ~90% identity between yeast and mammalian cytoplasmic actins (Galkin et al. 2002). Despite the clear differences between myosin and actin evolution, these two protein partners can be united under the umbrella of allostery. Structural polymorphism of F-actin manifests itself in multiple conformations of the D-loop (Merino et al. 2018; Pospich et al. 2020) and an allosteric coupling of its structural state with the structural state of the N- and C-termini of actin (Galkin et al. 2010). Based on the extreme conservation of internally buried residues within actin monomers and filaments, it seems reasonable that the conformational flexibility of actin filaments has provided the impetus for preserving the internal allosteric networks that is used by the myosin motors. This notion has a strong experimental support, since cross-linking of the two actin mobile elements (e.g., the D-loop and the C-terminus), completely abolishes force generation while allowing actomyosin interaction (Kim et al. 1998).

Overall, the very different evolutionary path was of myosin and actin forced the diverse family of myosin motors to use a very similar track on the surface of the evolutionary conserved actin filament (Robert-Paganin et al. 2020). This idea is beautifully illustrated by recently published cryo-EM structures of several quite diverse actomyosin complexes (Gurel et al. 2017; Mentes et al. 2018; Risi et al. 2021a; von der Ecken et al. 2016). In these complexes despite a very similar overall geometry of the actomyosin interface, the interaction of individual myosin actin binding elements differs between the isoforms (Figs. 14.10, 14.11, 14.12, 14.13, and 14.14). However, these structures were obtained only for the rigor state representing the end of the powerstroke (Fig. 14.5a, step 1). Therefore, near-atomic structures of

the weakly bound states (Fig. 14.5a, steps 4 and 5) of various actomyosin complexes are required to achieve a full molecular description of the myosin mechanochemical cycle.

Compliance with Ethical Standards Authors do not have any conflict of interests. Authors confirm that experiments described in the chapter involving humans or animals were conducted by respecting the corresponding ethical guidelines and that informed consent was obtained in case humans were involved. The work on this chapter work was financially supported by NIH grant R01 HL140925.

References

Adamek N, Coluccio LM, Geeves MA (2008) Calcium sensitivity of the cross-bridge cycle of , the adaptation motor in the inner ear. Proc Natl Acad Sci U S A 105(15):5710–5715

Alamo L, Qi D, Wriggers W, Pinto A, Zhu J, Bilbao A, Gillilan RE, Hu S, Padrón R (2016) Conserved intramolecular interactions maintain myosin interacting-heads motifs explaining tarantula muscle super-relaxed state structural basis. J Mol Biol 428(6):1142–1164

Al-Khayat HA, Kensler RW, Squire JM, Marston SB, Morris EP (2013) Atomic model of the human cardiac muscle myosin filament. Proc Natl Acad Sci U S A 110(1):318–323

Allen DG, Kentish JC (1985) The cellular basis of the length-tension relation in cardiac muscle. J Mol Cell Cardiol 17(9):821–840

Batters C, Arthur CP, Lin A, Porter J, Geeves MA, Milligan RA, Molloy JE, Coluccio LM (2004) Myo1c is designed for the adaptation response in the inner ear. EMBO J 23(7):1433–1440

Beach JR, Egelhoff TT (2009) Myosin II recruitment during cytokinesis independent of centralspindlin-mediated phosphorylation. J Biol Chem 284(40):27377–27383

Bement WM, Mooseker MS (1995) TEDS rule: a molecular rationale for differential regulation of myosins by phosphorylation of the heavy chain head. Cell Motil Cytoskeleton 31(2):87–92

Bershitsky SY, Tsaturyan AK, Bershitskaya ON, Mashanov GI, Brown P, Burns R, Ferenczi MA (1997) Muscle force is generated by myosin heads stereospecifically attached to actin. Nature 388(6638):186–190

Blanc F, Isabet T, Benisty H, Sweeney HL, Cecchini M, Houdusse A (2018) An intermediate along the recovery stroke of myosin VI revealed by X-ray crystallography and molecular dynamics. Proc Natl Acad Sci U S A 115(24):6213–6218

Bloemink MJ, Geeves MA (2011) Shaking the myosin family tree: biochemical kinetics defines four types of myosin motor. Semin Cell Dev Biol 22(9):961–967

Brenner SL, Korn ED (1983) On the mechanism of actin monomer-polymer subunit exchange at steady state. J Biol Chem 258(8):5013–5020

Brown JH, Kim KH, Jun G, Greenfield NJ, Dominguez R, Volkmann N, Hitchcock-DeGregori SE, Cohen C (2001) Deciphering the design of the tropomyosin molecule. Proc Natl Acad Sci U S A 98(15):8496–8501

Capitanio M, Canepari M, Cacciafesta P, Lombardi V, Cicchi R, Maffei M, Pavone FS, Bottinelli R (2006) Two independent mechanical events in the interaction cycle of skeletal muscle myosin with actin. Proc Natl Acad Sci U S A 103(1):87–92

Chen WT (1981) Mechanism of retraction of the trailing edge during fibroblast movement. J Cell Biol 90(1):187–200

Chou SZ, Pollard TD (2019) Mechanism of actin polymerization revealed by cryo-EM structures of actin filaments with three different bound nucleotides. Proc Natl Acad Sci U S A 116(10): 4265–4274

Clark R, Ansari MA, Dash S, Geeves MA, Coluccio LM (2005) Loop 1 of transducer region in mammalian class I myosin, Myo1b, modulates actin affinity, ATPase activity, and nucleotide access. J Biol Chem 280(35):30935–30942

Colson BA, Thompson AR, Espinoza-Fonseca LM, Thomas DD (2016) Site-directed spectroscopy of cardiac myosin-binding protein C reveals effects of phosphorylation on protein structural dynamics. Proc Natl Acad Sci U S A 113(12):3233–3238

Conibear PB, Bagshaw CR, Fajer PG, Kovacs M, Malnasi-Csizmadia A (2003) Myosin cleft movement and its coupling to actomyosin dissociation. Nat Struct Biol 10(10):831–835

Cope MJ, Whisstock J, Rayment I, Kendrick-Jones J (1996) Conservation within the myosin motor domain: implications for structure and function. Structure 4(8):969–987

Correia SS, Bassani S, Brown TC, Lisé M-F, Backos DS, El-Husseini A, Passafaro M, Esteban JA (2008) Motor protein-dependent transport of AMPA receptors into spines during long-term potentiation. Nat Neurosci 11(4):457–466

Coureux P-D, Wells AL, Ménétrey J, Yengo CM, Morris CA, Sweeney HL, Houdusse A (2003) A structural state of the myosin V motor without bound nucleotide. Nature 425(6956):419–423

Coureux P-D, Sweeney HL, Houdusse A (2004) Three myosin V structures delineate essential features of chemo-mechanical transduction. EMBO J 23(23):4527–4537

Courtemanche N (2018) Mechanisms of formin-mediated actin assembly and dynamics. Biophys Rev 10(6):1553–1569

De La Cruz EM, Ostap EM (2004) Relating biochemistry and function in the myosin superfamily. Curr Opin Cell Biol 16(1):61–67

De La Cruz EM, Wells AL, Sweeney HL, Ostap EM (2000) Actin and light chain isoform dependence of myosin V kinetics. Biochemistry 39(46):14196–14202

De La Cruz EM, Ostap EM, Sweeney HL (2001) Kinetic mechanism and regulation of myosin VI. J Biol Chem 276(34):32373–32381

Debold EP, Patlak JB, Warshaw DM (2005) Slip sliding away: load-dependence of velocity generated by skeletal muscle myosin molecules in the laser trap. Biophys J 89(5):L34–L36

Dobesh DP, Konhilas JP, de Tombe PP (2002) Cooperative activation in cardiac muscle: impact of sarcomere length. Am J Physiol Heart Circ Physiol 282(3):H1055–H1062

Dominguez R, Freyzon Y, Trybus KM, Cohen C (1998) Crystal structure of a vertebrate smooth muscle myosin motor domain and its complex with the essential light chain: visualization of the pre-power stroke state. Cell 94(5):559–571

Donovan KW, Bretscher A (2012) Myosin-V is activated by binding secretory cargo and released in coordination with Rab/exocyst function. Dev Cell 23(4):769–781

Drabikowski W, Kominz DR, Maruyama K (1968) Effect of troponin on the reversibility of tropomyosin binding to F-actin. J Biochem 63(6):802–804

Driska SP, Aksoy MO, Murphy RA (1981) Myosin light chain phosphorylation associated with contraction in arterial smooth muscle. Am J Phys 240(5):C222–C233

Ebashi S (1972) Calcium ions and muscle contraction. Nature 240(5378):217–218

Egelman EH (2001) Molecular evolution: actin's long lost relative found. Curr Biol 11(24):R1022–R1024

Eisenberg E, Hill TL (1985) Muscle contraction and free energy transduction in biological systems. Science 227(4690):999–1006

Fagarasanu A, Fagarasanu M, Eitzen GA, Aitchison JD, Rachubinski RA (2006) The peroxisomal membrane protein Inp2p is the peroxisome-specific receptor for the myosin V motor Myo2p of Saccharomyces cerevisiae. Dev Cell 10(5):587–600

Farmer SR, Wan KM, Ben-Ze'ev A, Penman S (1983) Regulation of actin mRNA levels and translation responds to changes in cell configuration. Mol Cell Biol 3(2):182–189

Ferenczi MA, Bershitsky SY, Koubassova N, Siththanandan V, Helsby WI, Panine P, Roessle M, Narayanan T, Tsaturyan AK (2005) The “roll and lock” mechanism of force generation in muscle. Structure 13(1):131–141

Fischer S, Windshügel B, Horak D, Holmes KC, Smith JC (2005) Structural mechanism of the recovery stroke in the myosin molecular motor. Proc Natl Acad Sci U S A 102(19):6873–6878

Fisher AJ, Smith CA, Thoden J, Smith R, Sutoh K, Holden HM, Rayment I (1995a) Structural studies of myosin:nucleotide complexes: a revised model for the molecular basis of muscle contraction. Biophys J 68:19S–26S

Fisher AJ, Smith CA, Thoden JB, Smith R, Sutoh K, Holden HM, Rayment I (1995b) X-ray structures of the myosin motor domain of Dictyostelium discoideum complexed with MgADP. BeFx and MgADP.AlF4. Biochemistry 34(28):8960–8972

Foth BJ, Goedecke MC, Soldati D (2006) New insights into myosin evolution and classification. Proc Natl Acad Sci U S A 103(10):3681–3686

Fujii T, Iwane AH, Yanagida T, Namba K (2010) Direct visualization of secondary structures of F-actin by electron cryomicroscopy. Nature 467(7316):724–728

Fujita-Becker S, Reubold TF, Holmes KC (2006) The actin-binding cleft: functional characterisation of myosin II with a strut mutation. J Muscle Res Cell Motil 27(2):115–123

Fujiwara I, Takahashi S, Tadakuma H, Funatsu T, Ishiwata S (2002) Microscopic analysis of polymerization dynamics with individual actin filaments. Nat Cell Biol 4(9):666–673

Furch M, Geeves MA, Manstein DJ (1998) Modulation of actin affinity and actomyosin adenosine triphosphatase by charge changes in the myosin motor domain. Biochemistry 37(18): 6317–6326

Galkin VE, VanLoock MS, Orlova A, Egelman EH (2002) A new internal mode in F-actin helps explain the remarkable evolutionary conservation of actin's sequence and structure. Curr Biol 12(7):570–575

Galkin VE, Orlova A, Schroder GF, Egelman EH (2010) Structural polymorphism in F-actin. Nat Struct Mol Biol 17(11):1318–1323

Galkin VE, Orlova A, Vos MR, Schröder GF, Egelman EH (2015) Near-atomic resolution for one state of F-actin. Structure (London, England: 1993) 23(1):173–182

Giese KC, Spudich JA (1997) Phenotypically selected mutations in myosin's actin binding domain demonstrate intermolecular contacts important for motor function. Biochemistry 36(28): 8465–8473

Greenberg MJ, Lin T, Goldman YE, Shuman H, Ostap EM (2012) Myosin IC generates power over a range of loads *via* a new tension-sensing mechanism. Proc Natl Acad Sci U S A 109(37): E2433–E2440

Greenberg MJ, Shuman H, Ostap EM (2014) Inherent force-dependent properties of β-cardiac myosin contribute to the force-velocity relationship of cardiac muscle. Biophys J 107(12):L41–L44

Gruen M, Prinz H, Gautel M (1999) cAPK-phosphorylation controls the interaction of the regulatory domain of cardiac myosin binding protein C with myosin-S2 in an on-off fashion. FEBS Lett 453(3):254–259

Guilford WH, Dupuis DE, Kennedy G, Wu J, Patlak JB, Warshaw DM (1997) Smooth muscle and skeletal muscle myosins produce similar unitary forces and displacements in the laser trap. Biophys J 72(3):1006–1021

Gurel PS, Kim LY, Ruijgrok PV, Omabegho T, Bryant Z, Alushin GM (2017) Cryo-EM structures reveal specialization at the myosin VI-actin interface and a mechanism of force sensitivity. eLife 6. https://doi.org/10.7554/eLife.31125.001

Hall ET, Dillard ME, Stewart DP, Zhang Y, Wagner B, Levine RM, Pruett-Miller SM, Sykes A, Temirov J, Cheney RE, Mori M, Robinson CG, Ogden SK (2021) Cytoneme delivery of Sonic Hedgehog from ligand-producing cells requires Myosin 10 and a Dispatched-BOC/CDON co-receptor complex. eLife 10:e61432

Harris DE, Work SS, Wright RK, Alpert NR, Warshaw DM (1994) Smooth, cardiac and skeletal muscle myosin force and motion generation assessed by cross-bridge mechanical interactions in vitro. J Muscle Res Cell Motil 15(1):11–19

Harris SP, Bartley CR, Hacker TA, McDonald KS, Douglas PS, Greaser ML, Powers PA, Moss RL (2002) Hypertrophic cardiomyopathy in cardiac myosin binding protein-C knockout mice. Circ Res 90(5):594–601

Hartman MA, Finan D, Sivaramakrishnan S, Spudich JA (2011) Principles of unconventional myosin function and targeting. Annu Rev Cell Dev Biol 27:133–155

Hawthorne JL, Mehta PR, Singh PP, Wong NQ, Quintero OA (2016) Positively charged residues within the MYO19 MyMOMA domain are essential for proper localization of MYO19 to the mitochondrial outer membrane. Cytoskeleton (Hoboken, NJ) 73(6):286–299

Heissler SM, Sellers JR (2014) Myosin light chains: Teaching old dogs new tricks. BioArchitecture 4(6):169–188

Heissler SM, Sellers JR (2016) Various themes of myosin regulation. J Mol Biol 428(9 Pt B):1927–1946

Heissler SM, Liu X, Korn ED, Sellers JR (2013) Kinetic characterization of the ATPase and actin-activated ATPase activities of Acanthamoeba castellanii myosin-2. J Biol Chem 288(37): 26709–26720

Herrera AM, McParland BE, Bienkowska A, Tait R, Paré PD, Seow CY (2005) 'Sarcomeres' of smooth muscle: functional characteristics and ultrastructural evidence. J Cell Sci 118(Pt 11): 2381–2392

Hill AV (1938) The heat of shortening and the dynamic constants of muscle. Proc R Soc B Biol Sci 126(843):136–195

Himmel DM, Gourinath S, Reshetnikova L, Shen Y, Szent-Gyorgyi AG, Cohen C (2002) Crystallographic findings on the internally uncoupled and near-rigor states of myosin: further insights into the mechanics of the motor. Proc Natl Acad Sci U S A 99(20):12645–12650

Holmes KC, Popp D, Gebhard W, Kabsch W (1990) Atomic model of the actin filament. Nature 347:44–49

Holt JR, Gillespie SKH, Provance DW, Shah K, Shokat KM, Corey DP, Mercer JA, Gillespie PG (2002) A chemical-genetic strategy implicates myosin-1c in adaptation by hair cells. Cell 108(3):371–381

Houdusse A, Sweeney HL (2016) How myosin generates force on actin filaments. Trends Biochem Sci 41(12):989–997

Houdusse A, Kalabokis VN, Himmel D, Szent-Gyorgyi AG, Cohen C (1999) Atomic structure of scallop myosin subfragment S1 complexed with MgADP: a novel conformation of the myosin head. Cell 97(4):459–470

Houdusse A, Szent-Gyorgyi AG, Cohen C (2000) Three conformational states of scallop myosin S1. Proc Natl Acad Sci U S A 97(21):11238–11243

Hu Z, Taylor DW, Reedy MK, Edwards RJ, Taylor KA (2016) Structure of myosin filaments from relaxed Lethocerus flight muscle by cryo-EM at 6 Å resolution. Sci Adv 2(9):e1600058

Huxley H, Hanson J (1954) Changes in the cross-striations of muscle during contraction and stretch and their structural interpretation. Nature 173(4412):973–976

Inchingolo AV, Previs SB, Previs MJ, Warshaw DM, Kad NM (2019) Revealing the mechanism of how cardiac myosin-binding protein C N-terminal fragments sensitize thin filaments for myosin binding. Proc Natl Acad Sci U S A 116(14):6828–6835

Ishikawa K, Catlett NL, Novak JL, Tang F, Nau JJ, Weisman LS (2003) Identification of an organelle-specific myosin V receptor. J Cell Biol 160(6):887–897

Ito K, Ikebe M, Kashiyama T, Mogami T, Kon T, Yamamoto K (2007) Kinetic mechanism of the fastest motor protein, Chara myosin. J Biol Chem 282(27):19534–19545

Jacobelli J, Estin Matthews M, Chen S, Krummel MF (2013) Activated T cell trans-endothelial migration relies on myosin-IIA contractility for squeezing the cell nucleus through endothelial cell barriers. PLoS One 8(9):e75151

Joel PB, Trybus KM, Sweeney HL (2001) Two conserved lysines at the 50/20-kDa junction of myosin are necessary for triggering actin activation. J Biol Chem 276(5):2998–3003

Jontes JD, Wilson-Kubalek EM, Milligan RA (1995) A 32 degree tail swing in brush border myosin I on ADP release. Nature 378(6558):751–753

Kabsch W, Mannherz HG, Suck D, Pai EF, Holmes KC (1990) Atomic structure of the actin:DNase I complex. Nature 347:37–44

Kensler RW, Stewart M (1983) Frog skeletal muscle thick filaments are three-stranded. J Cell Biol 96(6):1797–1802

Kim E, Bobkova E, Miller CJ, Orlova A, Hegyi G, Egelman EH, Muhlrad A, Reisler E (1998) Intrastrand cross-linked actin between Gln-41 and Cys-374. III. Inhibition of motion and force generation with myosin. Biochemistry 37(51):17801–17809

Kishino A, Yanagida T (1988) Force measurements by micromanipulation of a single actin filament by glass needles. Nature 334(6177):74–76

Kojima S, Konishi K, Katoh K, Fujiwara K, Martinez HM, Morales MF, Onishi H (2001) Functional roles of ionic and hydrophobic surface loops in smooth muscle myosin: their interactions with actin. Biochemistry 40(3):657–664

Kominz DR (1965) Mercurial-induced transformation of myosin prevented by adenosine triphosphate and pyrophosphate. Science 149(3690):1374–1375

Koppole S, Smith JC, Fischer S (2007) The structural coupling between ATPase activation and recovery stroke in the myosin II motor. Structure (London, England: 1993) 15(7):825–837

Korn ED (2000) Coevolution of head, neck, and tail domains of myosin heavy chains. Proc Natl Acad Sci 97(23):12559–12564

Kornberg TB, Roy S (2014) Cytonemes as specialized signaling filopodia. Development (Cambridge, England) 141(4):729–736

Kraft T, Mahlmann E, Mattei T, Brenner B (2005) Initiation of the power stroke in muscle: insights from the phosphate analog AlF4. Proc Natl Acad Sci U S A 102(39):13861–13866

Krendel M, Mooseker MS (2005) Myosins: tails (and heads) of functional diversity. Physiology 20(4):239–251

Kruppa AJ, Kishi-Itakura C, Masters TA, Rorbach JE, Grice GL, Kendrick-Jones J, Nathan JA, Minczuk M, Buss F (2018) Myosin VI-dependent actin cages encapsulate parkin-positive damaged mitochondria. Dev Cell 44(4):484–499.e6

Kuhner S, Fischer S (2011) Structural mechanism of the ATP-induced dissociation of rigor myosin from actin. Proc Natl Acad Sci U S A 108(19):7793–7798

Laakso JM, Lewis JH, Shuman H, Ostap EM (2008) Myosin I can act as a molecular force sensor. Science (New York, NY) 321(5885):133–136

Lauffenburger DA, Horwitz AF (1996) Cell migration: a physically integrated molecular process. Cell 84(3):359–369

Lee KH, Sulbarán G, Yang S, Mun JY, Alamo L, Pinto A, Sato O, Ikebe M, Liu X, Korn ED, Sarsoza F, Bernstein SI, Padrón R, Craig R (2018) Interacting-heads motif has been conserved as a mechanism of myosin II inhibition since before the origin of animals. Proc Natl Acad Sci U S A 115(9):E1991–E2000

Lehrer SS, Morris EP (1982) Dual effects of tropomyosin and troponin-tropomyosin on actomyosin subfragment 1 ATPase. J Biol Chem 257(14):8073–8080

Lewis JH, Greenberg MJ, Laakso JM, Shuman H, Ostap EM (2012) Calcium regulation of myosin-I tension sensing. Biophys J 102(12):2799–2807

Li G, Cui Q (2004) Analysis of functional motions in Brownian molecular machines with an efficient block normal mode approach: myosin-II and Ca2+ -ATPase. Biophys J 86(2):743–763

Lipatova Z, Tokarev AA, Jin Y, Mulholland J, Weisman LS, Segev N (2008) Direct interaction between a myosin V motor and the Rab GTPases Ypt31/32 is required for polarized secretion. Mol Biol Cell 19(10):4177–4187

Liu JCY, Rottler J, Wang L, Zhang J, Pascoe CD, Lan B, Norris BA, Herrera AM, Paré PD, Seow CY (2013) Myosin filaments in smooth muscle cells do not have a constant length. J Physiol 591(23):5867–5878

Llinas P, Isabet T, Song L, Ropars V, Zong B, Benisty H, Sirigu S, Morris C, Kikuti C, Safer D, Sweeney HL, Houdusse A (2015) How actin initiates the motor activity of Myosin. Dev Cell 33(4):401–412

Lombardi V, Piazzesi G, Ferenczi MA, Thirlwell H, Dobbie I, Irving M (1995) Elastic distortion of myosin heads and repriming of the working stroke in muscle. Nature 374(6522):553–555

Lorenz M, Holmes KC (2010) The actin-myosin interface. Proc Natl Acad Sci U S A 107(28): 12529–12534

Lu Q, Li J, Zhang M (2014) Cargo recognition and cargo-mediated regulation of unconventional myosins. Acc Chem Res 47(10):3061–3070

Luther PK, Winkler H, Taylor K, Zoghbi ME, Craig R, Padron R, Squire JM, Liu J (2011) Direct visualization of myosin-binding protein C bridging myosin and actin filaments in intact muscle. Proc Natl Acad Sci U S A 108(28):11423–11428

Margossian SS, Lowey S (1982) Preparation of myosin and its subfragments from rabbit skeletal muscle. Methods Enzymol 85(Pt B):55–71

Martyn DA, Regnier M, Xu D, Gordon AM (2001) Ca2+ - and cross-bridge-dependent changes in N- and C-terminal structure of troponin C in rat cardiac muscle. Biophys J 80(1):360–370

McConnell RE, Tyska MJ (2010) Leveraging the membrane - cytoskeleton interface with myosin-1. Trends Cell Biol 20(7):418–426

McKillop DFA, Geeves MA (1993) Regulation of the interaction between actin and myosin subfragment-1: evidence for three states of the thin filament. Biophys J 65:693–701

Mentes A, Huehn A, Liu X, Zwolak A, Dominguez R, Shuman H, Ostap EM, Sindelar CV (2018) High-resolution cryo-EM structures of actin-bound myosin states reveal the mechanism of myosin force sensing. Proc Natl Acad Sci U S A 115(6):1292–1297

Merino F, Pospich S, Funk J, Wagner T, Kullmer F, Arndt HD, Bieling P, Raunser S (2018) Structural transitions of F-actin upon ATP hydrolysis at near-atomic resolution revealed by cryo-EM. Nat Struct Mol Biol 25(6):528–537

Mihalyi E, Szent-Gyorgyi AG (1953) Trypsin digestion of muscle proteins. III. Adenosinetriphosphatase activity and actinbinding capacity of the digested myosin. J Biol Chem 201(1):211–219

Milligan RA (1996) Protein-protein interactions in the rigor actomyosin complex. Proc Natl Acad Sci U S A 93(1):21–26

Molinie N, Gautreau A (2018) The Arp2/3 Regulatory System and Its Deregulation in Cancer. Physiol Rev 98(1):215–238

Moss RL, Fitzsimons DP, Ralphe JC (2015) Cardiac MyBP-C regulates the rate and force of contraction in mammalian myocardium. Circ Res 116(1):183–192

Muretta JM, Rohde JA, Johnsrud DO, Cornea S, Thomas DD (2015) Direct real-time detection of the structural and biochemical events in the myosin power stroke. Proc Natl Acad Sci U S A 112(46):14272–14277

Nag S, Trivedi DV, Sarkar SS, Adhikari AS, Sunitha MS, Sutton S, Ruppel KM, Spudich JA (2017) The myosin mesa and the basis of hypercontractility caused by hypertrophic cardiomyopathy mutations. Nat Struct Mol Biol 24(6):525–533

Nagy NT, Sakamoto T, Takács B, Gyimesi M, Hazai E, Bikádi Z, Sellers JR, Kovács M (2010) Functional adaptation of the switch-2 nucleotide sensor enables rapid processive translocation by myosin-5. FASEB J 24(11):4480–4490

Nambiar R, McConnell RE, Tyska MJ (2009) Control of cell membrane tension by myosin-I. Proc Natl Acad Sci U S A 106(29):11972–11977

Oda T, Iwasa M, Aihara T, Maeda Y, Narita A (2009) The nature of the globular- to fibrous-actin transition. Nature 457(7228):441–445

Oeding SJ, Majstrowicz K, Hu X-P, Schwarz V, Freitag A, Honnert U, Nikolaus P, Bähler M (2018) Identification of Miro1 and Miro2 as mitochondrial receptors for myosin XIX. J Cell Sci 131(17):jcs219469

Onishi H, Mikhailenko SV, Morales MF (2006a) Toward understanding actin activation of myosin ATPase: the role of myosin surface loops. Proc Natl Acad Sci U S A 103(16):6136–6141

Onishi H, Mikhailenko SV, Morales MF (2006b) Toward understanding actin activation of myosin ATPase: the role of myosin surface loops. Proc Natl Acad Sci U S A 103(16):6136–6141

Parry DAD (1975) Analysis of the primary sequence of α-tropomyosin from rabbit skeletal muscle. J Mol Biol 98(3):519–535

Pasha SN, Meenakshi I, Sowdhamini R (2016) Revisiting myosin families through large-scale sequence searches leads to the discovery of new myosins. Evol Bioinformatics Online 12:201–211

Pearson RB, Jakes R, John M, Kendrick-Jones J, Kemp BE (1984) Phosphorylation site sequence of smooth muscle myosin light chain (Mr = 20 000). FEBS Lett 168(1):108–112
Perrin BJ, Ervasti JM (2010) The actin gene family: function follows isoform. Cytoskeleton 67(10): 630–634
Pollard TD (1986) Rate constants for the reactions of ATP- and ADP-actin with the ends of actin filaments. J Cell Biol 103(6 Pt 2):2747–2754
Pollard TD (2007) Regulation of actin filament assembly by Arp2/3 complex and formins. Annu Rev Biophys Biomol Struct 36:451–477
Pollard TD (2016) Actin and actin-binding proteins. Cold Spring Harb Perspect Biol 8(8):a018226
Pospich S, Merino F, Raunser S (2020) Structural effects and functional implications of phalloidin and jasplakinolide binding to actin filaments. Structure 28(4):437–449 e5
Previs MJ, Prosser BL, Mun JY, Previs SB, Gulick J, Lee K, Robbins J, Craig R, Lederer WJ, Warshaw DM (2015) Myosin-binding protein C corrects an intrinsic inhomogeneity in cardiac excitation-contraction coupling. Sci Adv 1(1):e1400205
Previs MJ, Mun JY, Michalek AJ, Previs SB, Gulick J, Robbins J, Warshaw DM, Craig R (2016) Phosphorylation and calcium antagonistically tune myosin-binding protein C's structure and function. Proc Natl Acad Sci U S A 113(12):3239–3244
Pylypenko O, Attanda W, Gauquelin C, Lahmani M, Coulibaly D, Baron B, Hoos S, Titus MA, England P, Houdusse AM (2013) Structural basis of myosin V Rab GTPase-dependent cargo recognition. Proc Natl Acad Sci U S A 110(51):20443–20448
Quintero OA, DiVito MM, Adikes RC, Kortan MB, Case LB, Lier AJ, Panaretos NS, Slater SQ, Rengarajan M, Feliu M, Cheney RE (2009) Human Myo19 is a novel myosin that associates with mitochondria. Curr Biol 19(23):2008–2013
Rayment I, Rypniewski WR, Schmidt-Base K, Smith R, Tomchick DR, Benning MM, Winkelmann DA, Wesenberg G, Holden HM (1993) Three-dimensional structure of myosin subfragment-1: a molecular motor. Science 261:50–57
Razumova MV, Shaffer JF, Tu AY, Flint GV, Regnier M, Harris SP (2006) Effects of the N-terminal domains of myosin binding protein-C in an in vitro motility assay: evidence for long-lived cross-bridges. J Biol Chem 281(47):35846–35854
Razumova MV, Bezold KL, Tu AY, Regnier M, Harris SP (2008) Contribution of the myosin binding protein C motif to functional effects in permeabilized rat trabeculae. J Gen Physiol 132(5):575–585
Reck-Peterson SL, Tyska MJ, Novick PJ, Mooseker MS (2001) The yeast class V myosins, Myo2p and Myo4p, are nonprocessive actin-based motors. J Cell Biol 153(5):1121–1126
Reubold TF, Eschenburg S, Becker A, Kull FJ, Manstein DJ (2003) A structural model for actin-induced nucleotide release in myosin. Nat Struct Biol 10(10):826–830
Risi C, Belknap B, Forgacs-Lonart E, Harris SP, Schroder GF, White HD, Galkin VE (2018) N-Terminal Domains of Cardiac Myosin Binding Protein C Cooperatively Activate the Thin Filament. Structure 26(12):1604–1611
Risi C, Schafer LU, Belknap B, Pepper I, White HD, Schroder GF, Galkin VE (2021a) High-resolution Cryo-EM structure of the cardiac actomyosin complex. Structure 29(1):50–60 e4
Risi CM, Pepper I, Belknap B, Landim-Vieira M, White HD, Dryden K, Pinto JR, Chase PB, Galkin VE (2021b) The structure of the native cardiac thin filament at systolic Ca(2+) levels. Proc Natl Acad Sci U S A 118(13):e2024288118
Robblee JP, Olivares AO, de la Cruz EM (2004) Mechanism of nucleotide binding to actomyosin VI: evidence for allosteric head-head communication. J Biol Chem 279(37): 38608–38617
Robert-Paganin J, Pylypenko O, Kikuti C, Sweeney HL, Houdusse A (2020) Force generation by myosin motors: a structural perspective. Chem Rev 120(1):5–35
Rohn JL, Patel JV, Neumann B, Bulkescher J, McHedlishvili N, McMullan RC, Quintero OA, Ellenberg J, Baum B (2014) Myo19 ensures symmetric partitioning of mitochondria and coupling of mitochondrial segregation to cell division. Curr Biol 24(21):2598–2605

Sanders TA, Llagostera E, Barna M (2013) Specialized filopodia direct long-range transport of SHH during vertebrate tissue patterning. Nature 497(7451):628–632
Sasaki N, Ohkura R, Sutoh K (2000) Insertion or deletion of a single residue in the strut sequence of Dictyostelium myosin II abolishes strong binding to actin. J Biol Chem 275(49):38705–38709
Sheetz MP (2001) Cell control by membrane-cytoskeleton adhesion. Nat Rev Mol Cell Biol 2(5): 392–396
Shih WM, Gryczynski Z, Lakowicz JR, Spudich JA (2000) A FRET-based sensor reveals large ATP hydrolysis-induced conformational changes and three distinct states of the molecular motor myosin. Cell 102(5):683–694
Shuman H, Greenberg MJ, Zwolak A, Lin T, Sindelar CV, Dominguez R, Ostap EM (2014) A vertebrate myosin-I structure reveals unique insights into myosin mechanochemical tuning. Proc Natl Acad Sci U S A 111(6):2116–2121
Smith CA, Rayment I (1996) X-ray structure of the magnesium(II).ADP.vanadate complex of the Dictyostelium discoideum myosin motor domain to 1.9 A resolution. Biochemistry 35(17): 5404–5417
Spudich JA (1994) How molecular motors work. Nature 372(6506):515–518
Stanganello E, Hagemann AIH, Mattes B, Sinner C, Meyen D, Weber S, Schug A, Raz E, Scholpp S (2015) Filopodia-based Wnt transport during vertebrate tissue patterning. Nat Commun 6: 5846
Sung J, Nag S, Mortensen KI, Vestergaard CL, Sutton S, Ruppel K, Flyvbjerg H, Spudich JA (2015) Harmonic force spectroscopy measures load-dependent kinetics of individual human β-cardiac myosin molecules. Nat Commun 6:7931
Suzuki Y, Yasunaga T, Ohkura R, Wakabayashi T, Sutoh K (1998) Swing of the lever arm of a myosin motor at the isomerization and phosphate-release steps. Nature 396(6709):380–383
Sweeney HL, Rosenfeld SS, Brown F, Faust L, Smith J, Xing J, Stein LA, Sellers JR (1998) Kinetic tuning of myosin *via* a flexible loop adjacent to the nucleotide binding pocket. J Biol Chem 273(11):6262–6270
Sweeney HL, Park H, Zong AB, Yang Z, Selvin PR, Rosenfeld SS (2007) How myosin VI coordinates its heads during processive movement. EMBO J 26(11):2682–2692
Takács B, O'Neall-Hennessey E, Hetényi C, Kardos J, Szent-Györgyi AG, Kovács M (2011) Myosin cleft closure determines the energetics of the actomyosin interaction. FASEB J 25(1): 111–121
Tehver R, Thirumalai D (2010) Rigor to post-rigor transition in myosin V: link between the dynamics and the supporting architecture. Structure (London, England: 1993) 18(4):471–481
Thomas DD, Ramachandran S, Roopnarine O, Hayden DW, Ostap EM (1995) The mechanism of force generation in myosin: a disorder-to-order transition, coupled to internal structural changes. Biophys J 68(4 Suppl):135S–141S
Toyoshima YY, Kron SJ, McNally EM, Niebling KR, Toyoshima C, Spudich JA (1987) Myosin subfragment-1 is sufficient to move actin filaments in vitro. Nature 328(6130):536–539
Tyska MJ, Mackey AT, Huang J-D, Copeland NG, Jenkins NA, Mooseker MS (2005) Myosin-1a is critical for normal brush border structure and composition. Mol Biol Cell 16(5):2443–2457
Uyeda TQ, Ruppel KM, Spudich JA (1994) Enzymatic activities correlate with chimaeric substitutions at the actin-binding face of myosin. Nature 368(6471):567–569
Van Dijk J, Furch M, Lafont C, Manstein DJ, Chaussepied P (1999) Functional characterization of the secondary actin binding site of myosin II. Biochemistry 38(46):15078–15085
Vandekerckhove J, Weber K (1978) Mammalian cytoplasmic actins are the products of at least two genes and differ in primary structure in at least 25 identified positions from skeletal muscle actins. Proc Natl Acad Sci U S A 75(3):1106–1110
Varkuti BH, Yang Z, Kintses B, Erdelyi P, Bardos-Nagy I, Kovacs AL, Hari P, Kellermayer M, Vellai T, Malnasi-Csizmadia A (2012) A novel actin binding site of myosin required for effective muscle contraction. Nat Struct Mol Biol 19(3):299–306
Veigel C, Coluccio LM, Jontes JD, Sparrow JC, Milligan RA, Molloy JE (1999) The motor protein myosin-I produces its working stroke in two steps. Nature 398(6727):530–533

Veigel C, Schmitz S, Wang F, Sellers JR (2005) Load-dependent kinetics of myosin-V can explain its high processivity. Nat Cell Biol 7(9):861–869

von der Ecken J, Muller M, Lehman W, Manstein DJ, Penczek PA, Raunser S (2015) Structure of the F-actin-tropomyosin complex. Nature 519(7541):114–117

von der Ecken J, Heissler SM, Pathan-Chhatbar S, Manstein DJ, Raunser S (2016) Cryo-EM structure of a human cytoplasmic actomyosin complex at near-atomic resolution. Nature 534(7609):724–728

Wagner W, Brenowitz SD, Hammer JA 3rd (2011) Myosin-Va transports the endoplasmic reticulum into the dendritic spines of Purkinje neurons. Nat Cell Biol 13(1):40–48

Wagner W, Lippmann K, Heisler FF, Gromova KV, Lombino FL, Roesler MK, Pechmann Y, Hornig S, Schweizer M, Polo S, Schwarz JR, Eilers J, Kneussel M (2019) Myosin VI drives clathrin-mediated AMPA receptor endocytosis to facilitate cerebellar long-term depression. Cell Rep 28(1):11–20.e9

Wang F, Thirumurugan K, Stafford WF, Hammer JA, Knight PJ, Sellers JR (2004) Regulated conformation of myosin V. J Biol Chem 279(4):2333–2336

Warshaw DM, Desrosiers JM, Work SS, Trybus KM (1990) Smooth muscle myosin cross-bridge interactions modulate actin filament sliding velocity in vitro. J Cell Biol 111(2):453–463

Wegner A (1976) Head to tail polymerization of actin. J Mol Biol 108(1):139–150

Wessels D, Murray J, Jung G, Hammer JA, Soll DR (1991) Myosin IB null mutants of Dictyostelium exhibit abnormalities in motility. Cell Motil Cytoskeleton 20(4):301–315

Whittaker M, Wilson-Kubalek EM, Smith JE, Faust L, Milligan RA, Sweeney HL (1995) A 35-A movement of smooth muscle myosin on ADP release. Nature 378(6558):748–751

Wong WW, Doyle TC, Reisler E (1999) Nonspecific weak actomyosin interactions: relocation of charged residues in subdomain 1 of actin does not alter actomyosin function. Biochemistry 38(4):1365–1370

Woodhead JL, Zhao F-Q, Craig R (2013) Structural basis of the relaxed state of a Ca2+-regulated myosin filament and its evolutionary implications. Proc Natl Acad Sci U S A 110(21): 8561–8566

Wriggers W, Schulten K (1999) Investigating a back door mechanism of actin phosphate release by steered molecular dynamics. Proteins 35(2):262–273

Wu XS, Rao K, Zhang H, Wang F, Sellers JR, Matesic LE, Copeland NG, Jenkins NA, Hammer JA (2002) Identification of an organelle receptor for myosin-Va. Nat Cell Biol 4(4):271–278

Wulf SF, Ropars V, Fujita-Becker S, Oster M, Hofhaus G, Trabuco LG, Pylypenko O, Sweeney HL, Houdusse AM, Schröder RR (2016) Force-producing ADP state of myosin bound to actin. Proc Natl Acad Sci U S A 113(13):E1844–E1852

Yamada A, Mamane A, Lee-Tin-Wah J, Di Cicco A, Prevost C, Levy D, Joanny JF, Coudrier E, Bassereau P (2014) Catch-bond behaviour facilitates membrane tubulation by non-processive myosin 1b. Nat Commun 5:3624

Yamada Y, Namba K, Fujii T (2020) Cardiac muscle thin filament structures reveal calcium regulatory mechanism. Nat Commun 11(1):153

Yamashita H, Sata M, Sugiura S, Momomura S, Serizawa T, Iizuka M (1994) ADP inhibits the sliding velocity of fluorescent actin filaments on cardiac and skeletal myosins. Circ Res 74(6): 1027–1033

Yang Y, Gourinath S, Kovács M, Nyitray L, Reutzel R, Himmel DM, O'Neall-Hennessey E, Reshetnikova L, Szent-Györgyi AG, Brown JH, Cohen C (2007) Rigor-like structures from muscle myosins reveal key mechanical elements in the transduction pathways of this allosteric motor. Structure (London, England: 1993) 15(5):553–564

Yang S, Lee KH, Woodhead JL, Sato O, Ikebe M, Craig R (2019) The central role of the tail in switching off 10S myosin II activity. J Gen Physiol 151(9):1081–1093

Yengo CM, De La Cruz EM, Safer D, Ostap EM, Sweeney HL (2002) Kinetic characterization of the weak binding states of myosin V. Biochemistry 41(26):8508–8517

Yumura S (1996) Rapid redistribution of myosin II in living Dictyostelium amoebae, as revealed by fluorescent probes introduced by electroporation. Protoplasma 192(3):217–227

Zhang J, Herrera AM, Paré PD, Seow CY (2010) Dense-body aggregates as plastic structures supporting tension in smooth muscle cells. Am J Physiol Lung Cell Mol Physiol 299(5):L631–L638

Zhang X, Kampourakis T, Yan Z, Sevrieva I, Irving M, Sun Y-B (2017) Distinct contributions of the thin and thick filaments to length-dependent activation in heart muscle. elife 6:e24081

Zhao F-Q, Craig R, Woodhead JL (2009) Head-head interaction characterizes the relaxed state of Limulus muscle myosin filaments. J Mol Biol 385(2):423–431